

POLITECNICO DI TORINO

Collegio di Ingegneria Energetica

**Corso di Laurea Magistrale in
Ingegneria Energetica e Nucleare**

Tesi di Laurea Magistrale

**Investigation of a saturation rule
for experimental fluxes
using a Neural Network approach**



Relatore

Prof. Fabio Subba

Candidato

Michele Fasciana

Marzo 2019

Abstract

Gyrokinetic transport solvers are powerful models that solve non-linear simulations to inform and help researchers involved in thermonuclear fusion development. One of the limitations of these codes is the computational cost. To face this problem, reduced models have been developed. Trapped Gyro-Landau Fluid (TGLF) model is a reduced model that computes the plasma turbulent fluxes inside the fusion reactors. The fluxes are computed using a quasi-linear approach. The non-linear fluxes are obtained with a saturation rule calibrated to fit a set of nonlinear gyrokinetic simulations.

An investigation on the saturation rule of the TGLF quasi-linear turbulent transport model has been performed. The turbulent fluxes obtained via TGLF are compared with the experimental fluxes inferred for experiments performed with the DIII-D National Fusion Facility.

A neural network based model for the TGLF saturation rule has been developed to link the quasi-linear quantities computed by TGLF to the experimentally inferred fluxes.

Contents

Abstract	iii
1 Introduction	1
1.1 What is fusion?	1
1.1.1 Basics of Nuclear Energy	2
1.1.2 Fusion Reactions	3
1.1.3 Physics of plasma	5
1.2 Magnetic confinement	7
1.2.1 Motion of particles in electromagnetic fields	7
1.2.2 Confinement machines	8
2 Plasma turbulence and solvers	11
2.1 Turbulence in plasma	11
2.2 TGLF	12
2.3 Experimental fluxes	16
2.4 TensorFlow workflow	18
2.5 How does a neural network work	18
3 Model a saturation rule with neural networks	23
3.1 Comparison of TGLF and experimental fluxes	23
3.2 Recalibration of SAT0	26
3.3 Modelling a saturation rule with a Neural Network approach	28
3.3.1 Reproduction of SAT0 with a Neural Network	28
3.3.2 Neural Network with SAT0 inputs	30
3.3.3 Neural Networks with plasma parameter inputs	33
4 Performances of the model and new saturation rule	39
4.1 Comparison of SAT0 and SATNN	39
4.2 Causes of SAT0 shortfall	43
4.3 New analytical saturation rule	44
5 Conclusions	49
Bibliography	53
A Coefficient of determination	55

List of Figures

1.1	Binding energy per nucleon. Source:[18]	2
1.2	Proton proton chain reaction. Source:[19]	3
1.3	Cross sections of eq. 1.5 reactions. Source:[6]	4
1.4	Lawson's criterion for D-T reaction. Source:[16]	5
1.5	Ideal circuit to study the Debye length. Source:[5]	6
1.6	Trajectory of a particle in a magnetic field. Source:[9]	8
1.7	Trajectory of a particle in a toroidal machine. Source:[16]	8
1.8	Typical tokamak magnetic system and resulting magnetic field. Source:[20]	10
1.9	Magnetic system and magnetic field of a Wendelstein stellarator. Source:[21]	10
2.1	Kolmogorov's law. Source:[11]	12
2.2	Magnetic surfaces in a plasma section.	13
2.3	GYRO electron temperature	14
2.4	TGLF energy flux equation. Colors match the quantities of figure 2.5	14
2.5	QL weight and saturation rule spectra.	15
2.6	Ions and energy fluxes computed with TGLF compared to the same quantities obtained with GYRO. Source:[8]	16
2.7	OMFIT workflow used to compute the experimental and TGLF fluxes.	17
2.8	Schematic of the TensorFlow graph that reproduces the TGLF calculations to obtain the fluxes.	18
2.9	Simple schematic of a Neural Network. The weights that links the nodes are indicated with the w_{nj} .	19
2.10	Training workflow of a neural network.	20
2.11	Schematic of the TensorFlow graph extended with the optimizer.	21
3.1	TGLF vs experimental energy fluxes of electrons.	24
3.2	TGLF vs experimental energy fluxes of ions.	24
3.3	TGLF vs experimental energy fluxes of electrons with histogram of the data.	25
3.4	TGLF vs experimental energy fluxes of ions with histogram of the data.	25
3.5	TGLF vs experimental energy fluxes of electrons after the ricalibration of the 4 free parameters.	27
3.6	TGLF vs experimental energy fluxes of ions after the ricalibration of the 4 free parameters.	27

3.7	Electron energy fluxes computed with saturation rule obtained with neural network compared to TGLF fluxes.	29
3.8	Ion energy fluxes computed with saturation rule obtained with neural network compared to TGLF fluxes.	30
3.9	Electron energy fluxes computed with saturation rule obtained with SATNN-multi compared to experimental fluxes.	31
3.10	Ion energy fluxes computed with saturation rule obtained with SATNN-multi compared to experimental fluxes.	31
3.11	Electron energy fluxes computed with saturation rule obtained with SATNN compared to experimental fluxes.	32
3.12	Ion energy fluxes computed with saturation rule obtained with SATNN compared to experimental fluxes.	33
3.13	Electron energy fluxes computed with saturation rule obtained with SATNN-multi compared to experimental fluxes.	35
3.14	Ion energy fluxes computed with saturation rule obtained with SATNN-multi compared to experimental fluxes.	35
3.15	Electron energy fluxes computed with saturation rule obtained with SATNN compared to experimental fluxes.	36
3.16	Ion energy fluxes computed with saturation rule obtained with SATNN compared to experimental fluxes.	36
3.17	Behavior of different saturation rules studied.	37
4.1	Highlight of the two different groups of energy fluxes and normalized distribution of the two group with respect to the electron temperature gradient.	40
4.2	\log_{10} of saturation rule SAT0 for all the database cases (a), for the cases with high value of the flux (b) and for the cases with low value of the flux(c)	41
4.3	Saturation rules SAT0 (left) and SATNN (right) for all the database cases (a)(d), for the cases with high value of the flux (b)(e) and for the cases with low value of the flux(c)(f)	42
4.4	\log_{10} behavior of the different saturation rules studied for a case with small gradient.	42
4.5	\log_{10} behavior of the different saturation rules studied for a case with high gradient.	43
4.6	Growth rates computed by TGLF with respect to the gradient.	44
4.7	Electrons energy fluxes computed with the analytic saturation rule compared to the experimental fluxes.	45
4.8	Ions energy fluxes computed with the analytic saturation rule compared to the experimental fluxes.	46
4.9	Behavior of the different saturation rules studied for a case with small gradient.	46
4.10	Behavior of the different saturation rules studied for a case with high gradient.	47
5.1	Electrons energy fluxes computed with the analytic saturation rule compared to the experimental fluxes.	50

5.2	Ions energy fluxes computed with the analytic saturation rule compared to the experimental fluxes.	51
5.3	QL weights computed by TGLF with respect to the gradient. . .	51

List of Tables

2.1	Parameters of the GA Standard Case	15
2.2	Coefficient of saturation rule 2.1c	15
3.1	Coefficient of saturation rule 3.1	26
3.2	List of inputs of SAT0.	29
3.3	Plasma Parameters	34

Chapter 1

Introduction

Electricity consumption growth is one of the main phenomena that we observe when we talk about the improvement of technology and the standard of living. With the increase of this demand some aspects related to the energy production must be taken into account. The most mature and economic affordable technologies to produce energy are:

- Conventional power plants that exploit fossil fuels such as coal, oil, and natural gas;
- Renewable energy, mainly solar and wind;
- Nuclear fission.

Each of these technologies has some weaknesses that encourage research toward different and better ways to produce energy.

Conventional power plants have the problem of fossil fuels consumption: their limited availability in the world and the pollution issues due to the greenhouse gases coming from the combustion of these fuels. Renewable energies have limited efficiency and availability that don't allow the use of them as base load energy production. Nuclear fission has the main difficulty in the management of long term radioactive waste produced inside the nuclear reactors. One of the alternatives to these methods is nuclear fusion.

1.1 What is fusion?

Nuclear fusion is the mechanism that exploit the combination of small atoms to create one or more different atoms and neutrons or protons. The most important system that work with fusion reactions is the Sun, and the stars in general. The fusion reactions release energy.

The goal of the fusion is the production of energy reproducing fusion mechanisms in particular reactors. The technology and the knowledge required are huge and this motivate scientist, researchers and companies to cooperate together to make fusion possible.

1.1.1 Basics of Nuclear Energy

Before talking about fusion, some basic concepts must be summarized in this paragraph.

Nuclear technologies exploit the reactions occurring between nuclei to produce energy. The energy of an atom is measured through the binding energy, that is the energy needed to split the nucleus into single nucleons (protons and neutrons).

It is obtained by the Einstein relationship:

$$\text{BindingEnergy} = \Delta E = \Delta mc^2 \quad (1.1)$$

where Δm , called the mass defect, represents the difference between the mass of the reactants and the mass of the products of the reactions and c represents the speed of light.

The mass defect is the difference between the sum of the masses of the nucleons that compose the nucleus and the mass of the nucleus itself, which is always smaller.

The behavior of the binding energy per nucleon is shown in figure 1.1:

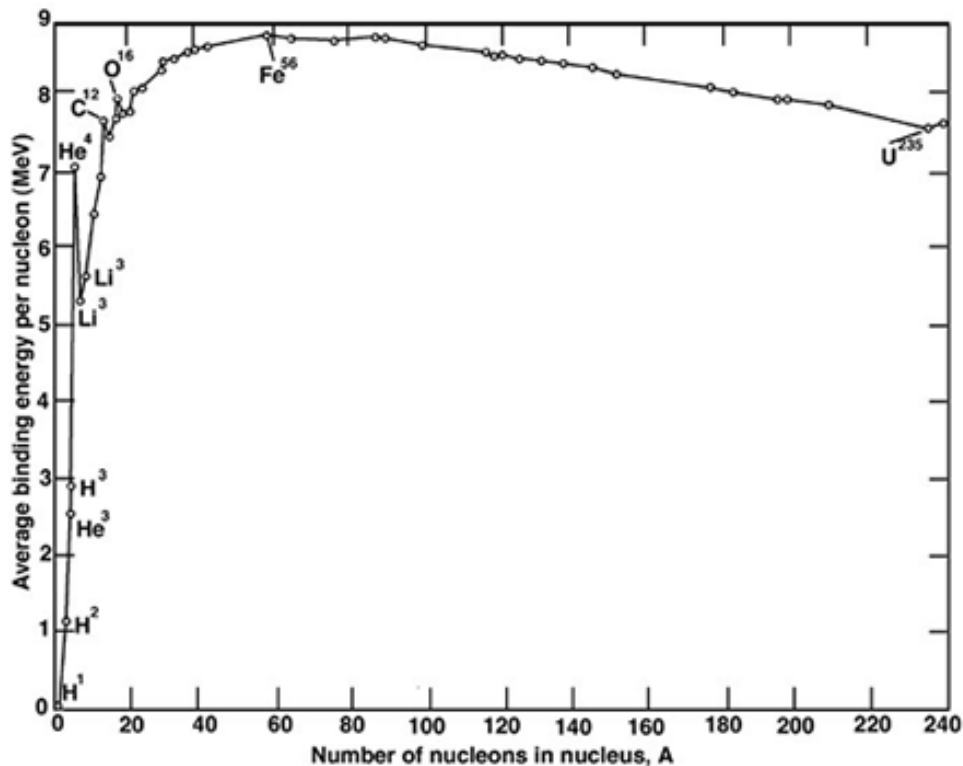


FIGURE 1.1: Binding energy per nucleon. Source:[18]

Fission exploits the separation of heavy nuclei that release kinetic energy due to the mass defect as outcome of the reaction. Fusion, on the other hand, exploits the combination of light atoms.

The typical energy released in these reactions are respectively 1MeV and 7 Mev.

Existing nuclear power plants use fission reactors due to the engineering feasibility, while fusion reactors are under research and development. Energy companies, governments, and researchers are investing resources and effort in fusion development because there are some advantages in terms of safety, environmental risk, and fuel reserve.

Fusion reactors are radioactive waste free; no long term radioactive elements are involved in the reactions.

The power density per unit of fuel is higher in fusion facilities and the fuel reserves are ensured for hundreds of years of operation.[5]

Concerning the safety aspects, there is no risk of chain reaction and, furthermore, no risk of proliferation, since only light elements are used.

1.1.2 Fusion Reactions

Fusion reactions exist in nature: they are the main processes that power celestial bodies.

In stars like the Sun, Helium is produced through the ‘proton proton chain’ based on three reactions:

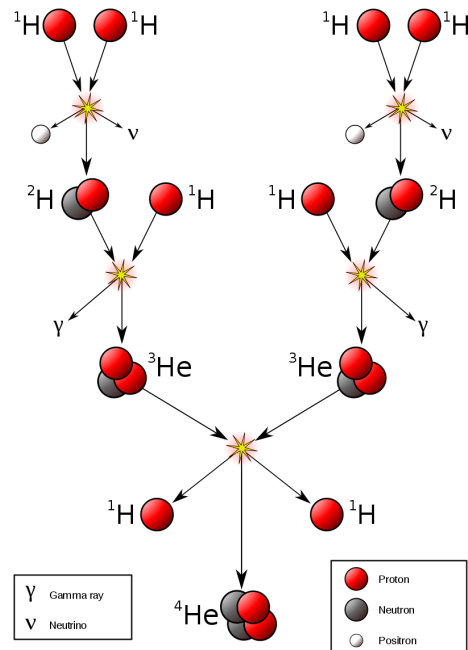
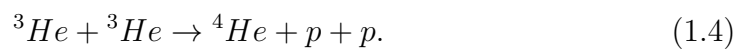


FIGURE 1.2: Proton proton chain reaction. Source:[19]

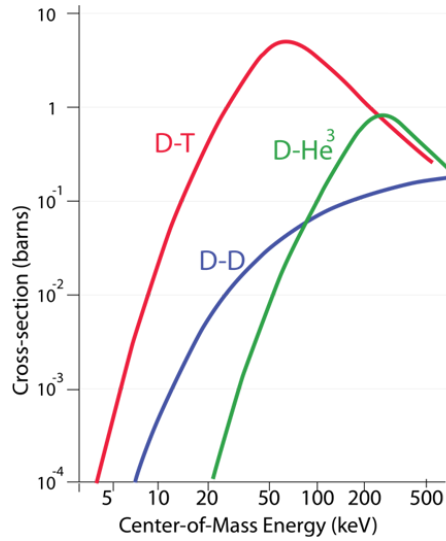
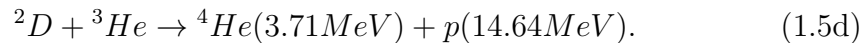
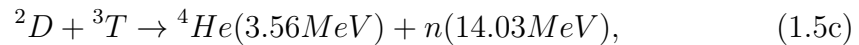
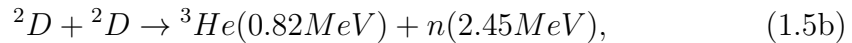
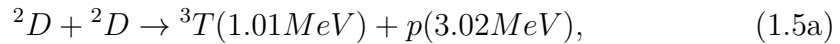


FIGURE 1.3: Cross sections of eq. 1.5 reactions. Source:[6]

On Earth these reactions cannot occur due to the different conditions of the environment. Here, fusion processes involve light elements such as Hydrogen (H), helium (He), and their isotopes; the main reactions are:



Inside the parentheses are the kinetic energies of the products.

In order to choose which of these reactions should be used in fusion reactors, the cross sections must be studied.

Figure 1.3 indicates that the Deuterium-Tritium reaction 1.5c has the higher value at the lowest energies. Hence, the D-T reaction is the most studied nowadays.

A fusion reactor can exploit the kinetic energy of the products to self-sustain the reaction and produce energy.

Deuterium is abundant in nature. There is 1 atom of D every 6500 atoms of Hydrogen in ocean waters. Using as reference the actual energy consumption rate it is estimated that deuterium can power the earth for the next 2 billion years.[5]

Tritium is radioactive, with a half-life of 12.3 years, so it can not be found in nature. It is obtained from Lithium 6, 6Li according to the reaction:



The abundance of ${}^6\text{Li}$ nowadays can ensure energy production for the next 20 000 years.[5]

In fusion reactors, there are different mechanisms that compete with energy production: gain of energy from the fusion reaction, losses due to Bremsstrahlung, thermal conduction, etc. The condition in which the losses are equal to the gain is called the “Ignition condition” and is the minimum threshold below which it is not possible to produce energy.

It is expressed as an inequality on the product of three important factors: the temperature T , the density n , and the energy confinement time τ_e

$$nT\tau_e > 10^{21} \text{keV s m}^{-3} \quad (1.7)$$

This inequality is well known as Lawson’s criterion and for D-T reaction is plotted in figure 1.4

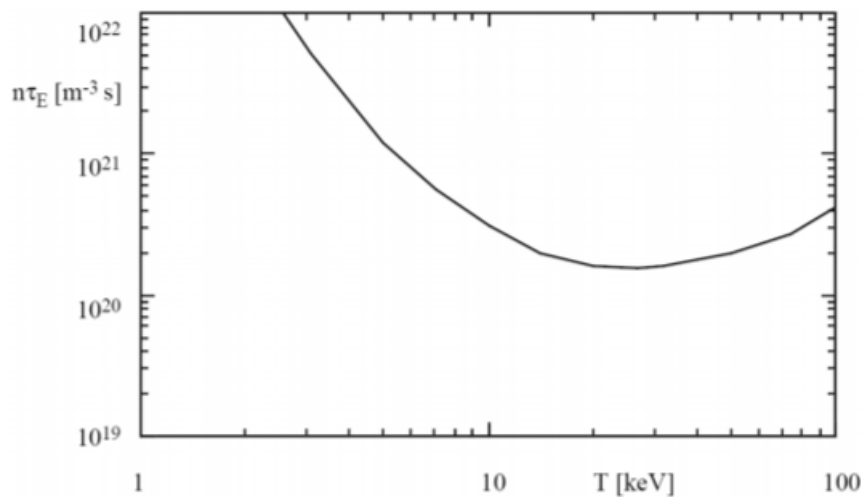


FIGURE 1.4: Lawson’s criterion for D-T reaction. Source:[16]

The minimum working temperature is 20 keV. Typical values of density and confinement time in a tokamak are respectively 10^{20} m^{-3} and 1 s.

1.1.3 Physics of plasma

In order to better understanding how a fusion reactor works a brief description of the plasma and how it behaves in electromagnetic fields is needed.

Plasma, also defined as the fourth state of the matter, is a fully ionized gas at high temperature. But this definition is not sufficient. A fully dissociated high temperature gas is defined as a plasma if its behavior is dominated by long-range electromagnetic interactions instead of short-range Coulomb collisions.

There are several parameters that could help to identify a plasma.

Since it is fully ionized the electrical neutrality must be maintained. Thus, if we imagine applying an electric potential to the plasma in a circuit shown in figure 1.5, the ions and electrons move in opposite directions and create small layers near the walls capable of shielding the potential.

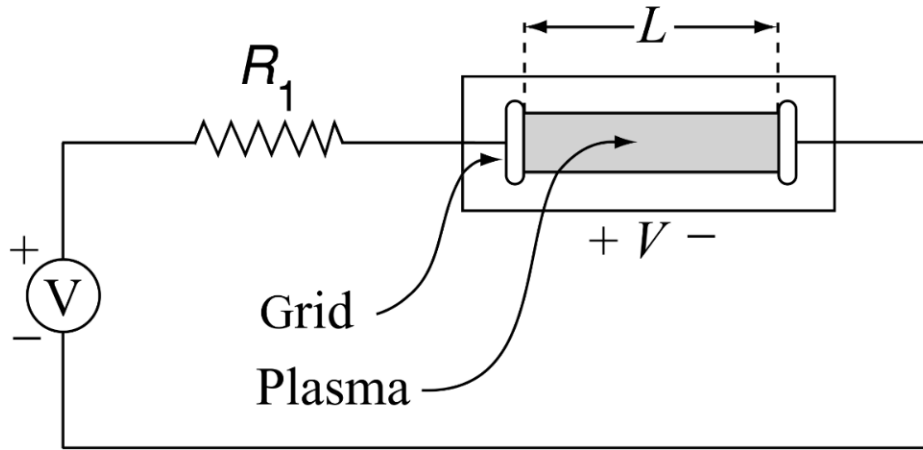


FIGURE 1.5: Ideal circuit to study the Debye length. Source:[5]

The length in which the potential drops to zero is called the *Debye length*. Plasmas require a very short Debye Length with respect to the typical one dimensional length that characterize the volume of a reactor and this requirement is fulfilled in all fusion plasma applications.

Ions and electrons have different masses. If an AC potential is applied to the same circuit (figure 1.5) can be noticed that the electrons react to the change of potential faster than the ions due to their smaller inertia. If a perturbation frequency is small both electrons and ions are capable to shielding out the AC field. Increasing the frequency, the ions are not able to follow the changes due to their inertia and if the frequency increases even more, also the electrons become slower than the periodic system modifications. Thus, there is a characteristic frequency defined as the Plasma Frequency, ω_p over which the plasma is no more able to screen out AC electric fields due to the inertia of the particles that compose it. In all fusion plasma applications the requirement $\omega \ll \omega_p$ is fulfilled so the properties of AC shielding are excellent.

Once the Debye Length defined, it is possible to define the Debye sphere as a sphere with the radius of a Debye Length. A sufficient number of particles should be contained inside the Debye sphere in order to smooth the current density into a continuous function. The parameter that controls the number of particles inside a Debye sphere is Λ_D and is defined as:

$$\Lambda_D = \frac{4\pi}{3} n_e \lambda_{De}^3 \gg 1 \quad (1.8)$$

Within the range of temperature and density of the plasma highlighted in paragraph 1.1.2 the Debye sphere density requirement is well respected.

In summary, the parameters and the constraint that characterize a fully ionized gas as plasma are:

- Debye length: $\lambda_D < \text{Characteristic Length of the reactor}$;
- Plasma frequency $\omega \ll \omega_p$;
- Number of particles in a Debye sphere $\gg 1$.

Fusion facilities, and specifically for our interest Tokamaks (see par. 1.2.2), confine charged particles by using electromagnetic fields.

1.2 Magnetic confinement

1.2.1 Motion of particles in electromagnetic fields

The motion of a particle with electrical charge q and mass m in a electromagnetic field is the combination of electrostatic and magnetic forces highlighted in the **Lorentz force law**

$$F = q(E + V \times B), \quad (1.9)$$

where q is the charge of the particle, qE is the electric force and $qV \times B$ is the magnetic force.

In the absence of the electrostatic field, the trajectory of the particle is the composition of two different components, one parallel to the magnetic field lines and one perpendicular.

In the perpendicular plane the particle rotates around the field line with a gyration radius ρ_s called the *Larmor radius* and a gyrofrequency ω_c .

$$\rho_s = \frac{mv_{\perp}}{|q|B} \quad (1.10)$$

$$\omega_c = \frac{|q|B}{m} \quad (1.11)$$

According to the formula 1.10 the radius increases as the energy of the particle increases. In the parallel direction the particle moves along the field line in a straight trajectory.

The sum of the two contributions results in an helicoidal trajectory along the field lines with opposite directions depending on the particle charge as shown in 1.6: The introduction of an electric field and non-homogeneous magnetic field (real case) lead the particle to suffer other drifts across the magnetic lines.

Knowing the behavior of a charged particle in a magnetic field the magnetic confinement can be introduced.

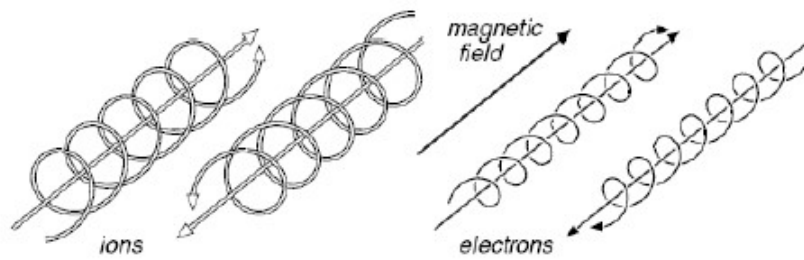


FIGURE 1.6: Trajectory of a particle in a magnetic field.
Source:[9]

1.2.2 Confinement machines

Cylindrical machines are able to confine the particles in the plane orthogonal to the magnetic field lines. To avoid the losses of particles at the edges, a closed configuration should be used. For this purpose toroidal configurations have been developed. The motion of particles is shown in figure 1.7.

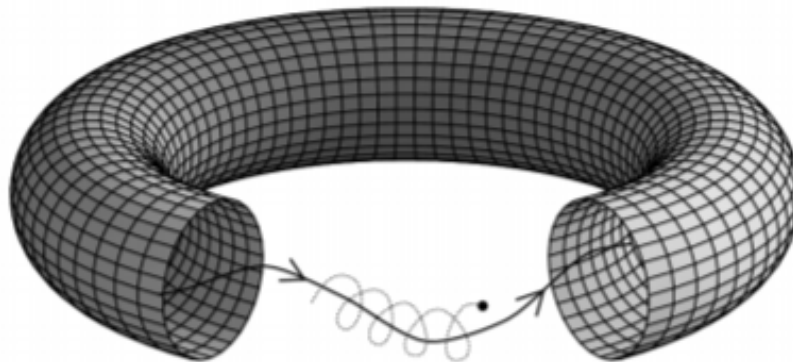


FIGURE 1.7: Trajectory of a particle in a toroidal machine.
Source:[16]

Particles are confined in the plane perpendicular to the magnetic field resulting in the helical trajectory discussed above. If the magnetic field lines are closed in a toroidal configuration, the particles can not escape since the lines are closed.

One setup of an axisymmetric toroidal device is the so called *tokamak*, contraction from Russian for “toroidal chamber with magnetic coils”. A tokamak produces two magnetic fields for the confinement of the plasma:

- Toroidal field generated using superconductor magnets or electromagnets. The current flows inside D-shaped Toroidal Field Coils and creates field lines along the toroidal direction;

- Poloidal field produced by the current flowing in the plasma. The current is induced in the plasma exploiting its resistivity: it behaves as the secondary winding of a transformer under the action of an external magnetic field.

The magnetic system is shown in figure 1.8.

To complete the discussion, another possible toroidal configuration is the stellarator. The main differences with respect to the tokamak are the non axisymmetry and the absence of the plasma current. A three-dimensional magnetic field is produced by a complex system of external coils as shown in figure 1.9.

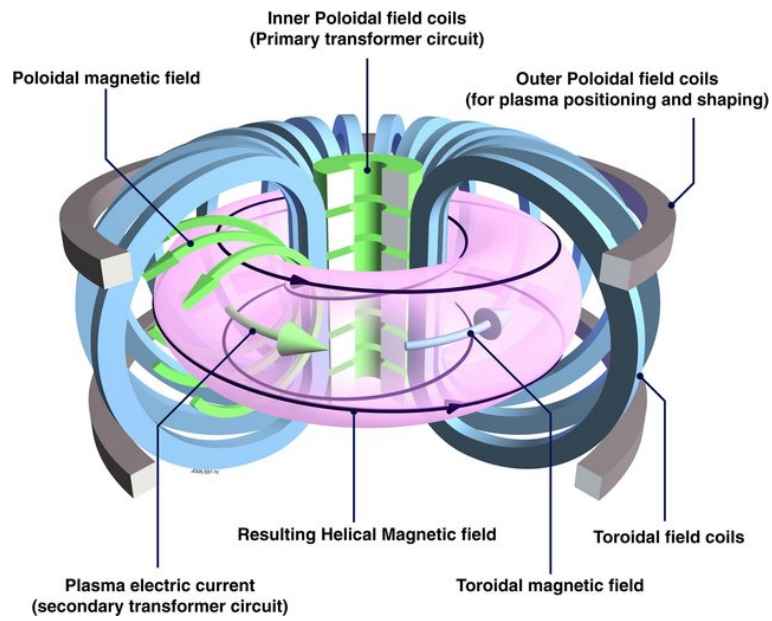


FIGURE 1.8: Typical tokamak magnetic system and resulting magnetic field. Source:[20]

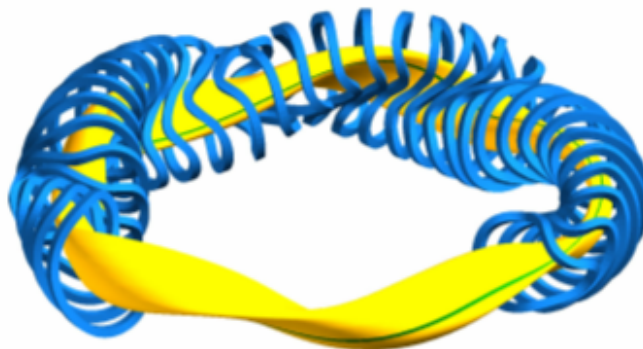


FIGURE 1.9: Magnetic system and magnetic field of a Wendelstein stellarator. Source:[21]

Chapter 2

Plasma turbulence and solvers

2.1 Turbulence in plasma

Turbulence is one of the most important problems that physics still cannot solve with a fully analytical approach. Turbulent phenomena occur everyday in our lives.

Some example of turbulence are the flowing of water, wind motion, and all of the other phenomena related to the chaotic behavior of fluids and gases.

Nowadays, it is impossible to have an exact mathematical definition of turbulence. But there are some basic principles gleaned through history:

- the processes occurring in a turbulent system are irreversible and random;
- turbulence results in fluctuations at various wavenumber scales;
- energy is transferred among these fluctuation scales.

Turbulence give rise to eddies that carry energy, particles, or momentum, and these eddies also create smaller eddies of comparable scale. The process occurs at each wavenumber scale starting from the largest, identified as k_0 , to the last small wavenumber, k_D .

The energy is transferred with a power law well known as Kolmogorov's law. Figure 2.1 shows the energy spectrum as function of the wavenumber: under the Kolmogorov scale, k_D , viscosity causes the conversion of the transferred energy into heat.

If the injection of energy balances the dissipation of heat, the system reaches the saturation of the turbulence.

This thesis is focused on how these saturation phenomena are formulated by transport models.

The turbulence in plasma is studied to understand its behavior. The goal of fusion is to reach the break-even point, that is the threshold above which the energy produced in a tokamak is greater than the energy injected to heat up the plasma.

In an early stage the instabilities had a big effects on the performance of fusion machines. With the improvement of designs and the introduction of new technologies it was possible to mitigate the macroinstabilities producing hotter and more stable plasmas.

The transport models that describe the plasma are based on a diffusion mechanism: collisions between particles drive these to move across the magnetic lines.

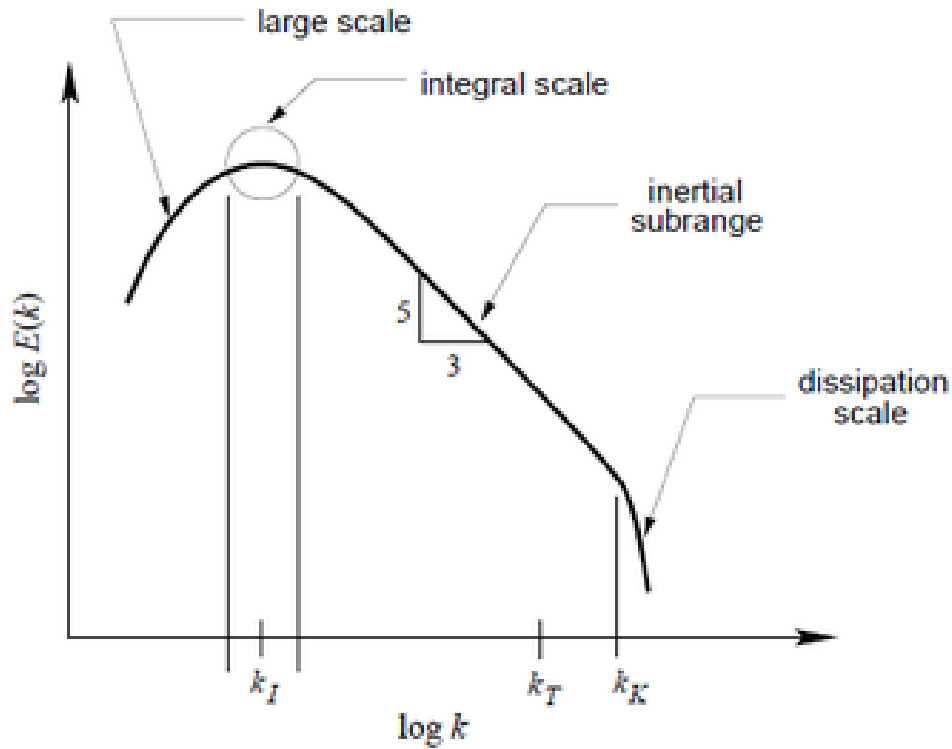


FIGURE 2.1: Kolmogorov's law. Source:[11]

The characteristic length of the step is comparable with the Larmor radius of the particles themselves.

But with the increasing of the performance the plasma becomes more collisionless and the neoclassical theory – which is identified with the toroidally modified Coulomb collision causes of transport – produces estimations of fluxes different from those inferred experimentally.

Other mechanisms act as driver of the turbulence in the hotter plasma scenarios. These mechanisms are generated by the small scale fluctuations that, in particular modes, can interact and create transport of energy and particles.

2.2 TGLF

The transport inside the plasma moves particles and energy from the center toward the edge of the tokamak reactors.

As can be seen in figure 2.2, in a section perpendicular to the toroidal direction the magnetic surfaces are closed and particles and energy can be transferred from the core to the sides since the density and temperature profiles evolve in radial direction.

Different models were developed to quantify the fluxes inside tokamaks. GYRO [1][2][3] is a transport model that performs fully nonlinear gyrokinetic simulations. It was used to create a database used to calibrate reduced transport models. Notwithstanding success in its results, GYRO has a huge computational cost that make the calculations slow and not useful for control or regulation of future machines.

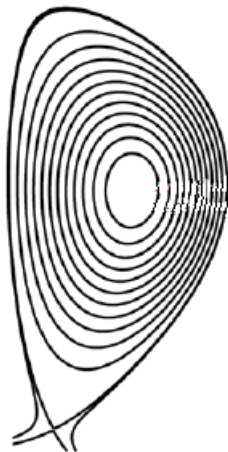


FIGURE 2.2: Magnetic surfaces in a plasma section.

To face the problem, reduced models based on theory have been developed. These models solve different equations than the fully gyro-kinetic equations, making some assumptions and simplifying the complexity of the problem. One of these codes is TGLF. As the name suggests, it models Trapped Gyro-Landau Fluid equations.[15][14][8]

TGLF solves a system of 15 equations and finds the linear eigenmodes for the drift-wave instabilities that are used to compute the quasi-linear (QL) weights. [14] The name quasi-linear comes from the nature of the model in that it uses a quasi-linear approach to approximate the non-linear turbulent fluxes. The QL weights correspond each mode at each wavenumber solved by TGLF and are related to the perturbations of electrostatic potential, temperature, and density.

TGLF computes a so called saturation rule to link the QL weights to the turbulent non-linear fluxes. The QL quantities and the saturation rule refer to a single mode and are local in the normalized poloidal wavenumber \hat{k}_y , defined as $\hat{k}_y = k_y \rho_s = nq/r$ where n is the toroidal mode number, q the safety factor, and r the minor radius in the midplane.

TGLF obtains the non linear fluxes integrating over all the k_y contributions using the two most unstable modes.

The QL weights and the saturation rule are defined as

$$Q = \frac{3}{2} \sum_{\hat{k}_y} p c_s \left[\frac{\text{Re}(i \hat{k}_y \tilde{\Phi}^* \tilde{p}_T)}{\sum_a \tilde{V}_a^* \tilde{V}_a} \right] \bar{V}^2, \quad (2.1a)$$

$$\Gamma = \sum_{\hat{k}_y} n c_s \left[\frac{\text{Re}(i \hat{k}_y \tilde{\Phi}^* \tilde{n})}{\sum_a \tilde{V}_a^* \tilde{V}_a} \right] \bar{V}^2, \quad (2.1b)$$

$$\bar{V}^2 = C_{norm} \left(\frac{\rho_s \hat{\omega}_{d0}}{a \hat{k}_y} \right)^2 \left(1 + \frac{T_e}{T_i} \right)^2 (\bar{\gamma}_{net}^{C_1} + C_2 \bar{\gamma}_{net}) \frac{1}{\hat{k}_y^{C_3}}. \quad (2.1c)$$

where a is the species index, \tilde{V}_a is the total eigenvector computed by TGLF solving the moment equations, $\tilde{\Phi} = e\tilde{\phi}/T_e$ is the normalized electrostatic potential fluctuation, and γ_{net} is the net linear growth rate

Equations 2.1a and 2.1b are the fluxes of energy and particles respectively and contains inside the square brackets the definition of the QL weights. The equation 2.1c is the saturation rule used to link the QL weights to the non-linear turbulent fluxes.

Figure 2.3 shows the electron temperature fluctuation at a point inside the plasma computed with a GYRO simulation.

Figure 2.5 shows the behavior of the QL weight (blue), the saturation rule (green), and the product of the two (red) in the \hat{k}_y space.

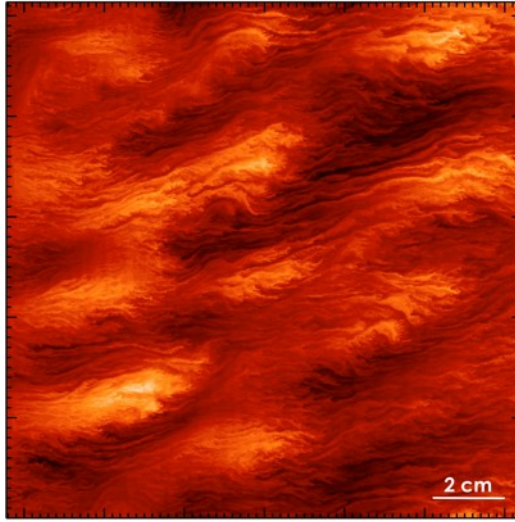


FIGURE 2.3: GYRO electron temperature

$$Q = \frac{3}{2} \sum_{\hat{k}_y} \left[\frac{\text{Re}(i\hat{k}_y \tilde{\Phi}^* \tilde{p}_T)}{\sum_a \tilde{V}_a^* \tilde{V}_a} \right] \bar{V}^2$$

FIGURE 2.4: TGLF energy flux equation. Colors match the quantities of figure 2.5

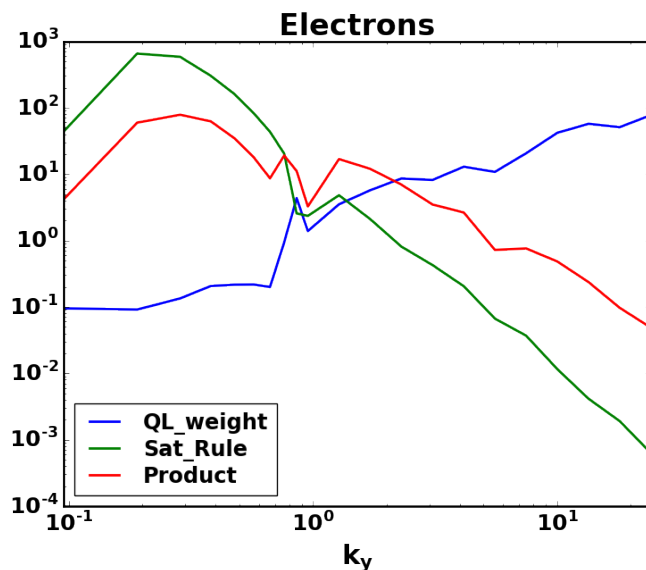


FIGURE 2.5: QL weight and saturation rule spectra.

Equation 2.1c is the functional form of the saturation rule SAT0.[8] It was obtained calibrating 4 free parameters: C_{norm} , C_1 , C_2 and C_3 . The calibration was performed to fit the energy fluxes of a database of simulations computed using the GYRO code. The GYRO Nonlinear Gyrokinetic Simulation Database [7] is a database of 82 simulations performed around the so-called GA Standard Case (GA-STD). The parameters for the GA-STD are highlighted in table 2.1.

TABLE 2.1: Parameters of the GA Standard Case

$R/a = 3.0$	$r/a = 0.5$	$q = 2$
$\hat{s} = 1.0$	$\beta = 0$	$\alpha = 0$
$a/L_n = 1.0$	$a/L_T = 3.0$	$T_i/T_e = 1.0$
$\nu_{ei}(a/c_s) = 0.0$	$\gamma_E(a/c_s) = 0.0$	$\gamma_p(a/c_s) = 0.0$

The GYRO calibrated values of the free parameters of SAT0 (2.1c) are:

TABLE 2.2: Coefficient of saturation rule 2.1c

C_{norm}	32.48
C_1	1.547
C_2	0.543
C_3	1.25

The term $1/\hat{k}_y^{C_3}$ is applied only for values of $\hat{k}_y \geq 1$, which means high- k modes.

TGLF reproduces well the electron and ion energy fluxes obtained with GYRO as shown in figure 2.6.

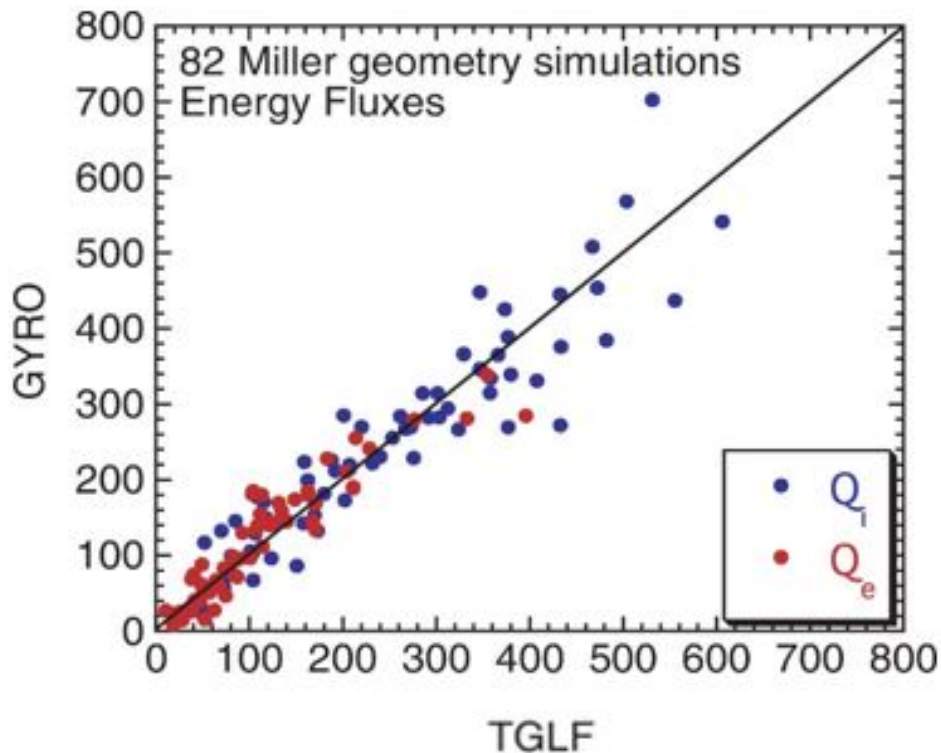


FIGURE 2.6: Ions and energy fluxes computed with TGLF compared to the same quantities obtained with GYRO. Source:[8]

2.3 Experimental fluxes

Since the aim of the thesis is the comparison of the TGLF fluxes and the experimental fluxes, a brief workflow to compute the experimental fluxes is discussed. To analyze the relations between the above mentioned quantities, a dataset of TGLF and corresponding experimental fluxes is needed.

The data analysis are performed using the OMFIT integrated modeling framework [12]. “One Modeling Framework for Integrated Tasks (OMFIT) is a comprehensive integrated modeling framework which has been developed to enable physics codes to interact in complicated workflows, and support scientists at all stages of the modeling cycle.[12]”

In this framework, it is possible to solve the power balance equation

$$\frac{\partial T}{\partial t} + \nabla Q = S$$

combining the profile fitting, equilibria reconstruction, and source terms obtained with different modules in OMFIT. [12]

The profile fitting is computed with the OMFITprofiles module [10] And the equilibrium reconstruction is facilitated by the EFITtime module.

Solving the power balance, given the sources, it is possible to obtain the experimental fluxes. Using the plasma parameters obtained with the profile fitting it is possible to run TGLF simulations for the same cases and obtain the corresponding theoretical turbulent fluxes.

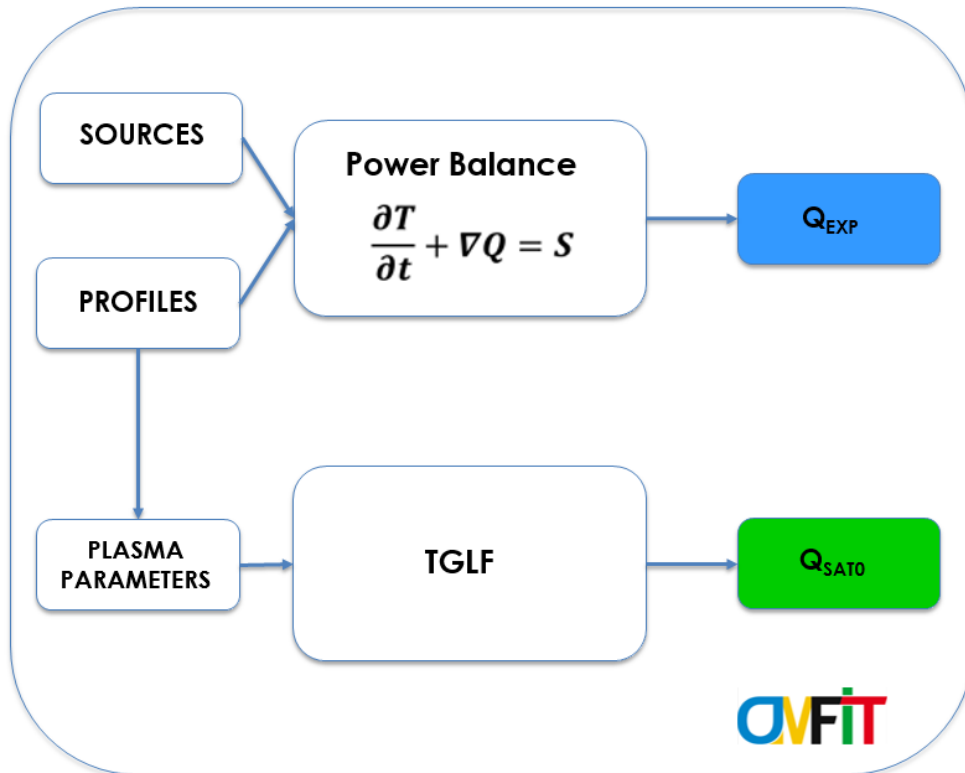


FIGURE 2.7: OMFIT workflow used to compute the experimental and TGLF fluxes.

For the purpose of this thesis more than 60000 cases of 780 different DIII-D [4] discharges with the following characteristics have been collected:

- the shots are DIII-D discharges;
- for each shot the default settings of OMFIT have been used;
- in the plasma there are 3 thermal species: electrons, deuterium, carbon;
- for each shot 9 time slices were considered in the range 2000 to 2800 *ms* with a uniform step of 100 *ms*;
- for each time slice 9 radii were considered in the range $\rho = 0.1$ to 0.9 with a uniform step of 0.1, where ρ is a flux surface label (normalized toroidal flux).

In figure 2.7 a scheme of the workflow is shown.

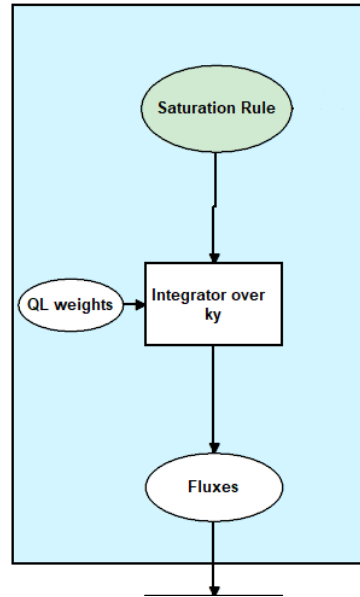


FIGURE 2.8: Schematic of the TensorFlow graph that reproduces the TGLF calculations to obtain the fluxes.

2.4 TensorFlow workflow

The evaluations and the development of the investigation of saturation rules have been performed using the TensorFlow (TF) library that is an open-source library developed and released by Google and used in machine learning applications such as Neural Networks.

The main feature of TF is the modular architecture: it works with a graph structure of the code in which it is possible to substitute one single module leaving the rest of the program fixed.

The TensorFlow library was used via the python language. The reference modular graph used for all of the evaluations reproduces the TGLF operations to compute the fluxes as shown in figure 2.8.

The QL weights are multiplied by the saturation rule and integrated over the \hat{k}_y spectra to obtain the TGLF non-linear turbulent fluxes.

2.5 How does a neural network work

As mentioned in the previous paragraph, the TensorFlow library was used to reproduce the TGLF code. The modularity was exploited to exchange the formulation of the saturation rule Eq. (2.1c) with a new module that evaluate this quantity via a neural network.

To proceed in the analysis a brief introduction on machine learning and neural network is presented below.

Machine learning is a branch of computer science that develops algorithms to perform specific tasks without being explicitly programmed. The framework used for these kinds of algorithms is the neural network.

The idea behind the neural network is contained in the name itself: a neural

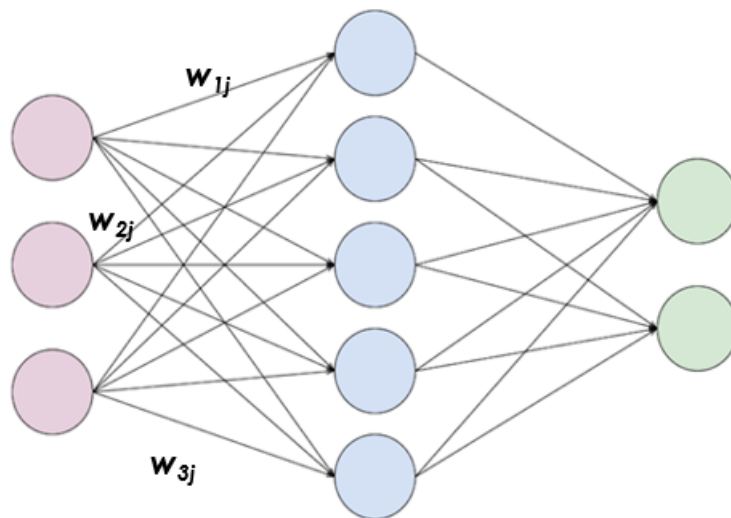


FIGURE 2.9: Simple schematic of a Neural Network. The weights that links the nodes are indicated with the w_{nj} .

network algorithm tries to simulate the synapses of a human brain to learn mathematical processes or make a prediction without the use of specific - and explicit - code.

A neural network is composed of a set of nodes, called artificial neurons, linked together by connections like in a human brain. The output of each node is a real number obtained by a non-linear combination of the inputs. The outputs are multiplied by a so-called *weight*, that adjusts the value of the output, amplifying or reducing it.

A typical architecture of a neural network consists in various layers, each being composed of a certain number of nodes. The first layer is called the *input layer* and has a number of nodes equal to the number of inputs to the neural network; the last layer is the *output layer* that has the number of nodes equal to the number of outputs that is desired. In between one or more *hidden layers* can be implemented. The more difficult the problem is to solve, the more complex the network architecture is. An example of a neural network is shown in figure 2.9. This example network has 3 inputs, 1 hidden layer of 5 nodes, and two outputs.

To obtain a meaningful network, the network should be 'trained'. The training is the most important process. In fact, during the training, the values of the weights, hence the connections between the nodes, are updated to find the right relations between input and output data.

The training consists of successive iterations, called *epochs*, where the values of the weights are modified in a process described in figure 2.10.

The neural network weights are initialized to random values at the first epoch. Using these values the neural network computes the outputs starting from the input data. The outputs are compared with known target values and the error is computed. Thanks to backpropagation, the weights are updated to minimize

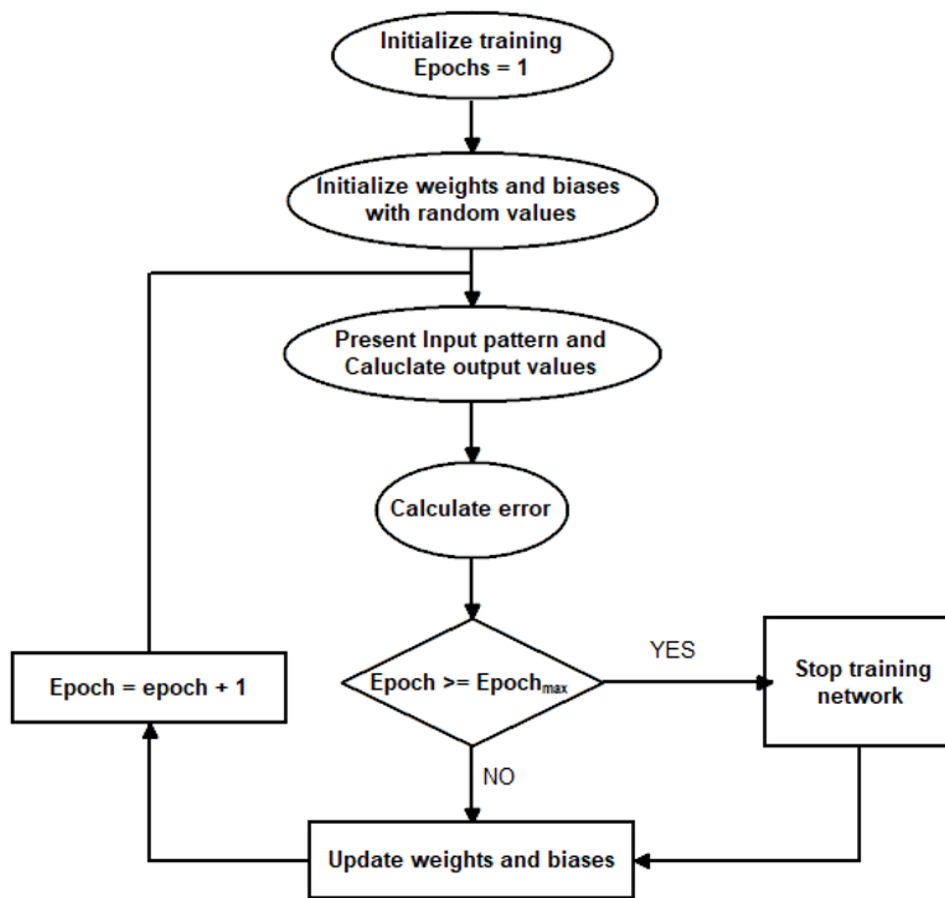


FIGURE 2.10: Training workflow of a neural network.

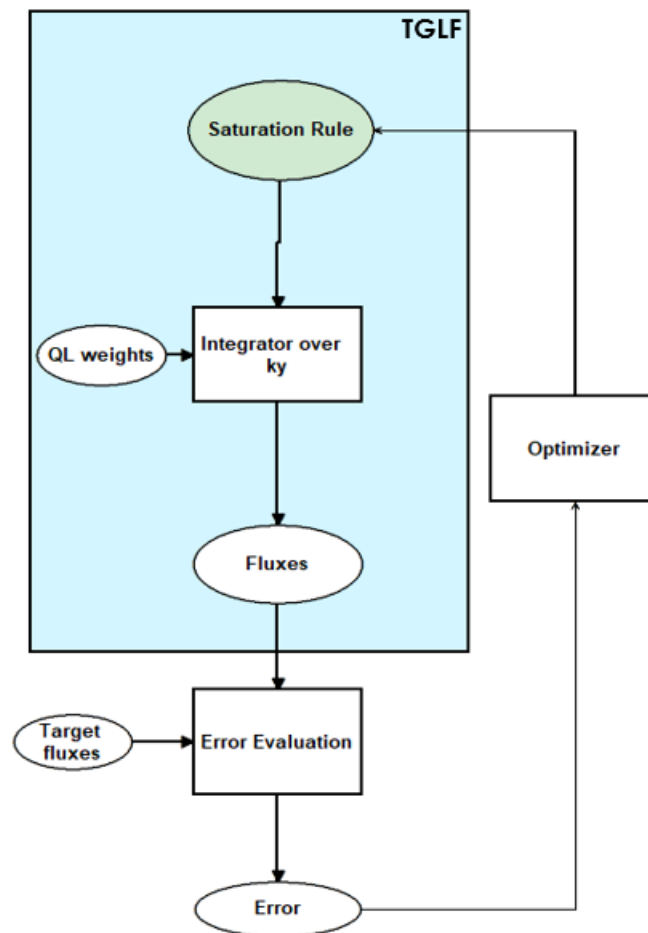


FIGURE 2.11: Schematic of the TensorFlow graph extended with the optimizer.

the error at the following epoch. Specifically, the update is performed computing the gradient of the error with respect to the weights. The optimization process ends when the error reaches a desired small value or when the number of epochs exceeds a fixed value.

Having in mind the basic principle of a neural network, the reference graph 2.8 has been extended by adding a module that computes the error comparing the computed fluxes with the target values of fluxes in the database.

The error is used in an optimization function to correct the evaluation of the saturation rule. The final goal is the minimization of the error.

The extended workflow is shown in figure 2.11.

Chapter 3

Model a saturation rule with neural networks

In this chapter the saturation rule is studied to understand the relationship between the QL weights and the inferred experimental fluxes.

SAT0 was obtained calibrating 4 parameters to fit a set of energy fluxes obtained with GYRO.(paragraph 2.2)

The performances of TGLF using SAT0 are good in the prediction of the theoretical turbulent fluxes. A comparison with the experimental fluxes will be performed to test how TGLF results are different with respect to these fluxes. After the comparison, a recalibration of the four SAT0 free parameters is performed to improve the results and finally a neural network approach is used to find a new functional form of the saturation rule.

All the analysis are performed on the electrons and ions energy fluxes since the saturation rule SAT0 was calibrated reducing the error estimated on these two quantities. The ions energy flux is the sum of the energy flux of all of the ion species in the plasma.

3.1 Comparison of TGLF and experimental fluxes

The theoretical nature of the saturation rule leads to the investigation of how the results obtained with TGLF are able to reproduce the experimental results. The database used is the one discussed in paragraph 2.3.

The experimental fluxes compared to the TGLF fluxes for the same cases are shown in figure 3.1 for the electron energy fluxes and in figure 3.2 for the ion energy fluxes.

A better projection of the data can be done using an histogram plot. Figures 3.3 and 3.4 show the same information as figures 3.1 and 3.2 but highlight the density of the data in each point of the plot.

The sparsity of the points indicates that there is a bad correlation between the TGLF and the experimental energy fluxes for all the species inside the reactor.

As can be noticed, there is an anomalous concentration of points in the lower part of the plot for both electron and ion energy fluxes. Specifically, TGLF underestimates the value of the fluxes concentrated in this zone.

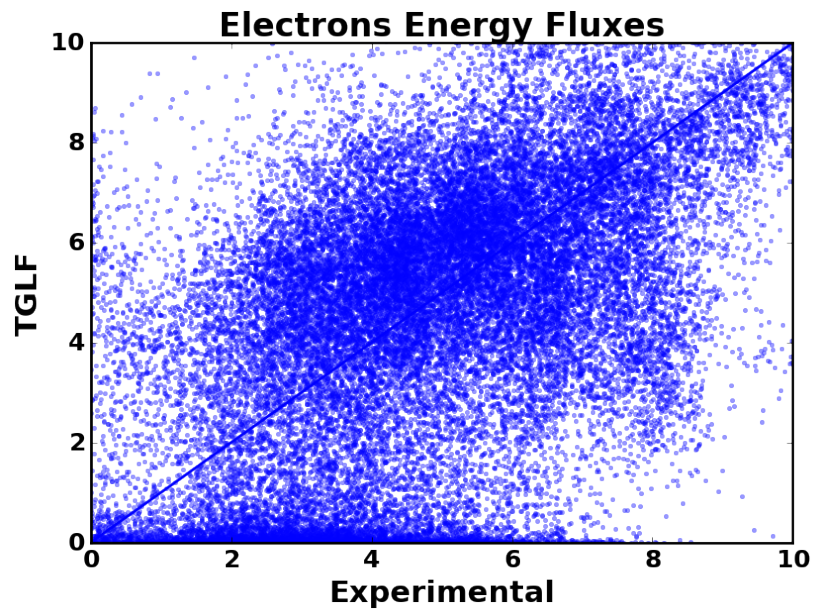


FIGURE 3.1: TGLF vs experimental energy fluxes of electrons.

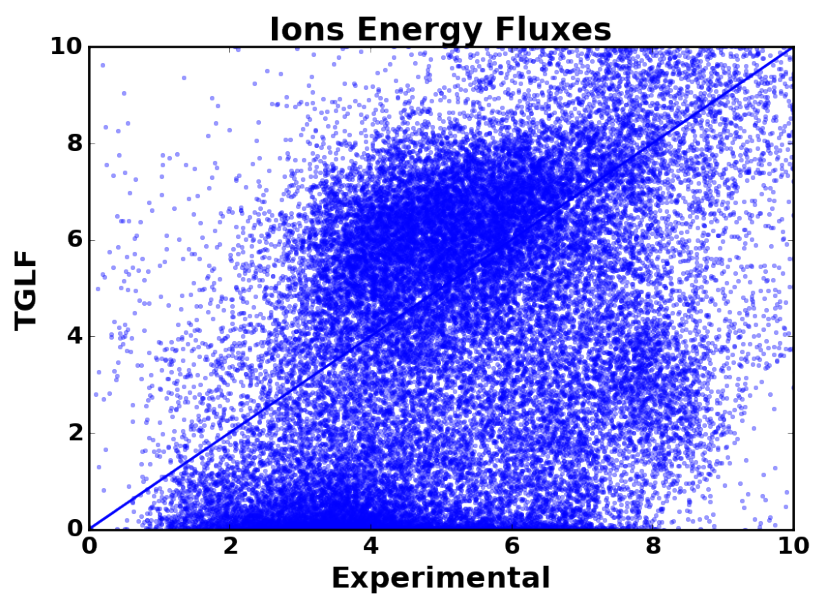


FIGURE 3.2: TGLF vs experimental energy fluxes of ions.

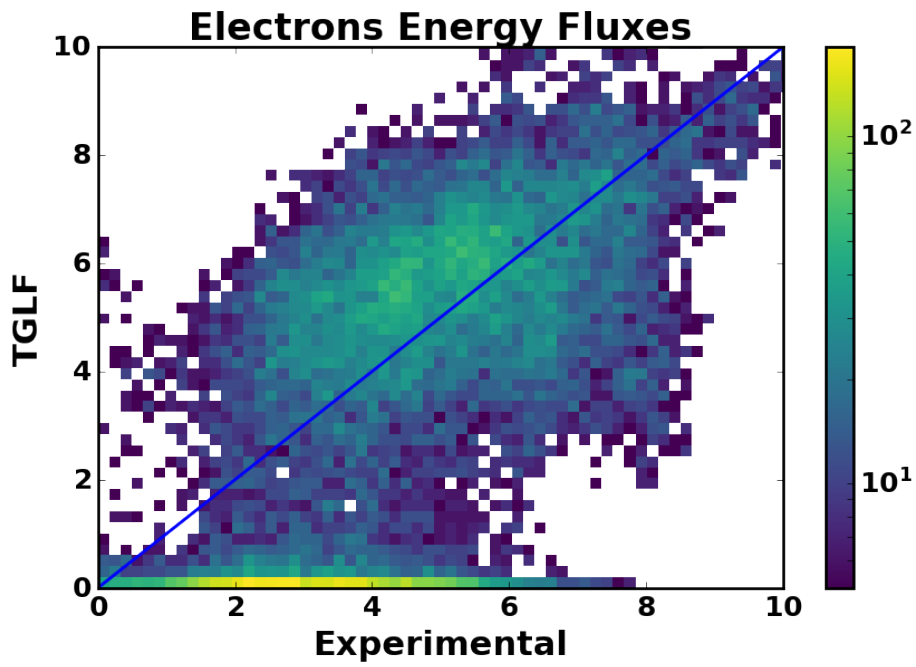


FIGURE 3.3: TGLF vs experimental energy fluxes of electrons with histogram of the data.

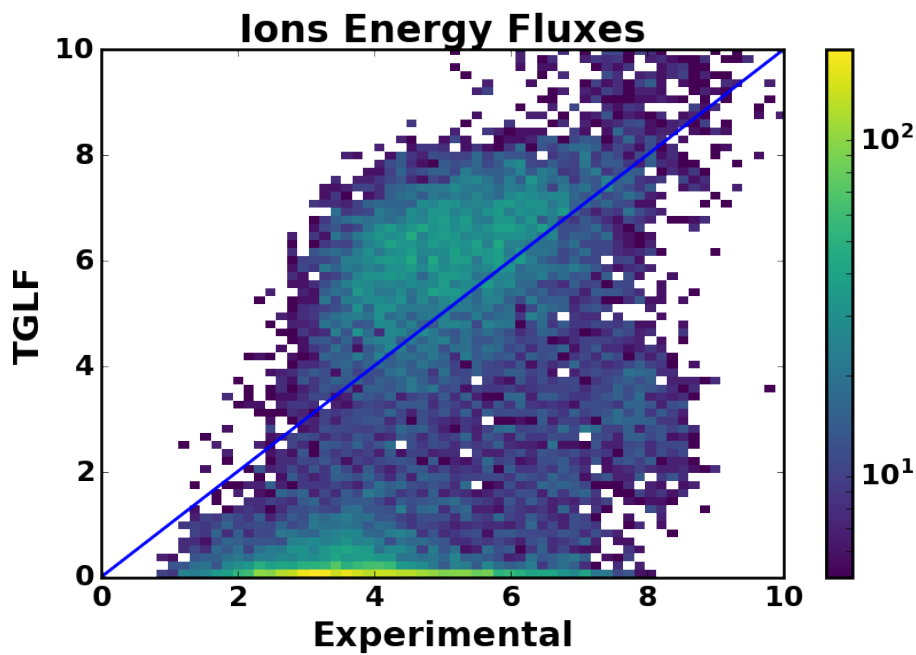


FIGURE 3.4: TGLF vs experimental energy fluxes of ions with histogram of the data.

3.2 Recalibration of SAT0

The comparison of the TGLF fluxes with respect to the experimental fluxes shows a mismatching of the values. To face the problem, the saturation rule can be studied since it was calibrated to fit theoretical simulations – runs of the GYRO code.

Knowing the values of the experimental fluxes a similar procedure can be followed.

The functional form of SAT0 contains four parameters that can be changed to recalibrate the saturation rule to fit the experimental results.

The recalibration is performed trying to reduce the error between the experimental fluxes and the fluxes computed using the SAT0 saturation rule. The parameters are highlighted in the following formula:

$$\bar{V}^2 = C_{norm} \left(\frac{\rho_s \hat{\omega}_{d0}}{a \hat{k}_y} \right)^2 \left(1 + \frac{T_e}{T_i} \right)^2 (\bar{\gamma}_{net}^{C_1} + C_2 \bar{\gamma}_{net}) \frac{1}{\hat{k}_y^{C_3}}. \quad (3.1)$$

Using the flowchart described in figure 2.11 the four parameters can be updated at each epoch. After the recalibration the new values of the coefficients are:

TABLE 3.1: Coefficient of saturation rule 3.1

<i>coefficient</i>	<i>SAT0</i>	<i>Recalibrated</i>
C_{norm}	32,48	32,33
C_1	1.547	0.6
C_2	0.543	0.0046
C_3	1.25	1.55

The values of the coefficient C_1 and C_2 that influence the growth rates γ_{net} are reduced. This trend will be discussed later.

The results of the energy fluxes after the recalibration are shown in figures 3.5 for electrons and 3.6 for ions.

The new values of fluxes using the new coefficients 3.1 do not fit the experimental fluxes. The recalibration is not effective in the fitting of the experimental fluxes. The underestimation of the fluxes is still present for both electrons and ions. A deep investigation in the relationship between theoretical and experimental values is needed because changing the free parameters is not sufficient to improve the performance of the saturation rule. The theoretical SAT0 is not able to fit the experimental data with a simple recalibration suggesting the need for a different approach to find a new functional form that better estimates the experimental fluxes.

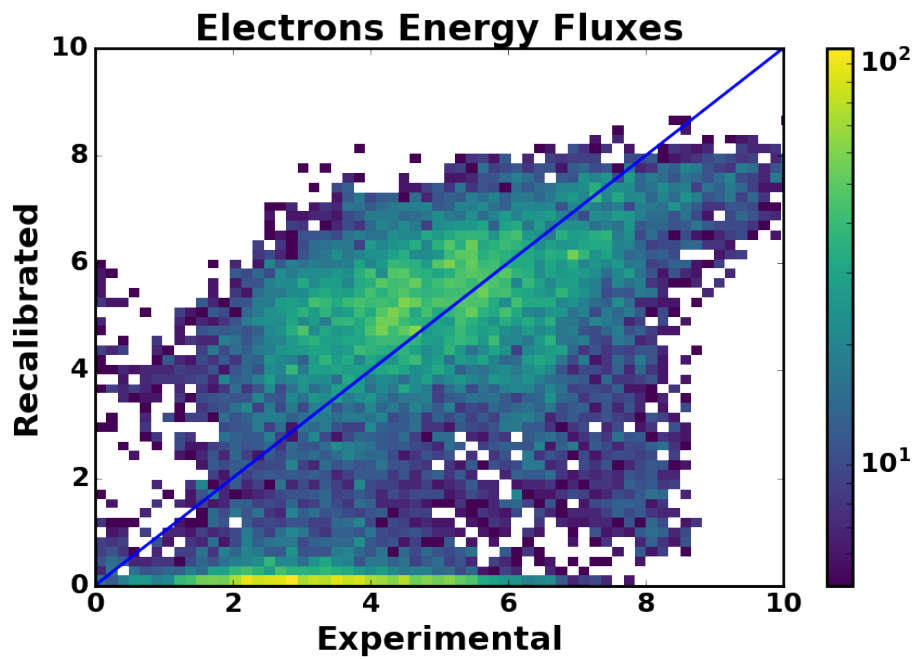


FIGURE 3.5: TGLF vs experimental energy fluxes of electrons after the ricalibration of the 4 free parameters.

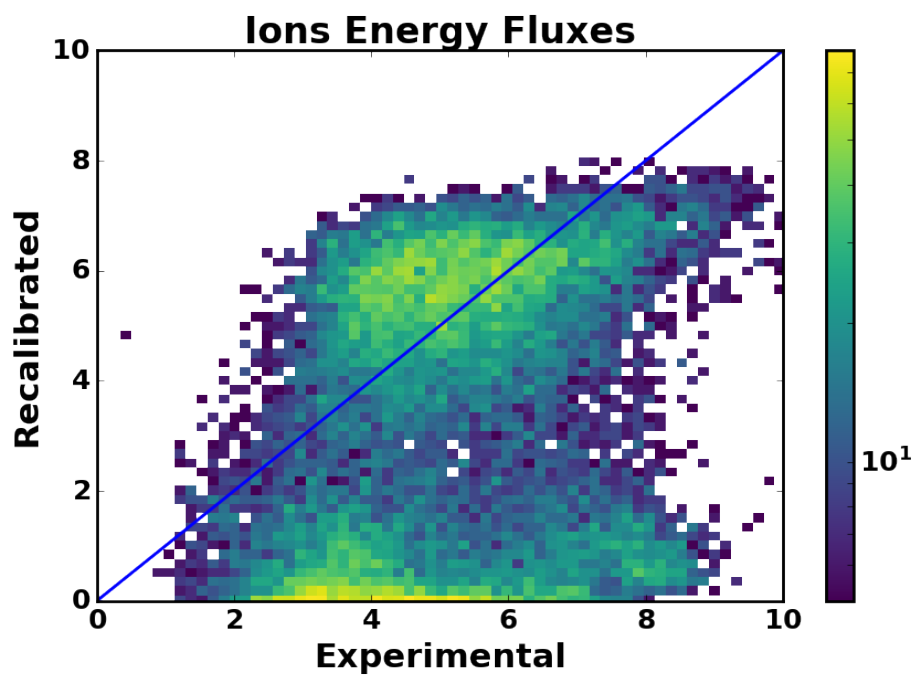


FIGURE 3.6: TGLF vs experimental energy fluxes of ions after the ricalibration of the 4 free parameters.

3.3 Modelling a saturation rule with a Neural Network approach

The functional form of SAT0 (2.1c) was obtained to fit 82 GYRO simulations. The recalibration of the four free parameters to fit the experimental fluxes is not effective and TGLF with the recalibrated saturation rule is not able to reproduce the experimental fluxes. These shortfalls in the SAT0 model are studied in the following paragraphs.

A fully theoretical approach can be used to model the saturation rule. But this approach needs a deep understanding and knowledge of the plasma physics and transport phenomenology. This could require years of investigation and experience.

A faster approach can be found in the use of machine learning and neural network algorithms. Although this method could give results yielding a good model that matches the experimental fluxes, the reliability of the model may not be satisfactory since physics constraints cannot be respected and the model could produce a non physical meaning.

But the use of the neural network to find results and hints useful to drive the theoretical research, finding new correlations of the data, can be an efficient tool to improve the understanding of the plasma physics, and, in particular, to find a model for the saturation rule in TGLF that better reproduces the experimental fluxes.

3.3.1 Reproduction of SAT0 with a Neural Network

A neural network can be used to model the saturation rule to link the QL weight computed by TGLF to the turbulent fluxes.

The first step of the study is the reproduction of the TGLF fluxes using the neural network to find the formulation of the saturation rule.

Having in mind the workflow 2.11 discussed in paragraph 2.4 the block of the saturation rule can be substituted with a neural network algorithm that computes the values of the saturation rule.

The saturation rule SAT0 is local in wavenumber \hat{k}_y spectrum. The default of TGLF is set to have a spectrum with 21 values of the poloidal wavenumber. To obtain the fluxes TGLF computes the contribution of the two most unstable modes leading to 42 values of SAT0 for each case.

This setup guided the choice of the topology of the neural network.

Each single value for each k_y is computed by a single neural network. The output of the multi neural network architecture, SATNN-multi, that contains 42 neural networks, is a set of 42 values of V^2 , one for each value of \hat{k}_y .

The inputs of the neural network are the same of the SAT0 and are highlighted in table 3.2:

TABLE 3.2: List of inputs of SAT0.

Parameter	Value
\hat{k}_y	normalized poloidal wavenumber $k_\theta \rho_s$
γ_{net}	net linear growth rate
T_e/T_i	Electron to ion temperature ratio
R/a	normalized major radius

The saturation rule obtained with the neural networks is used to compute the energy fluxes. These fluxes are compared to the fluxes computed by TGLF to minimize the error and train the neural network.

In figures 3.7 and 3.8 is shown the result of the TensorFlow workflow 2.8. On the x axis there are the TGLF fluxes and on the y axis there are the values of fluxes computed using the SATNN-multi to compute the saturation rule.

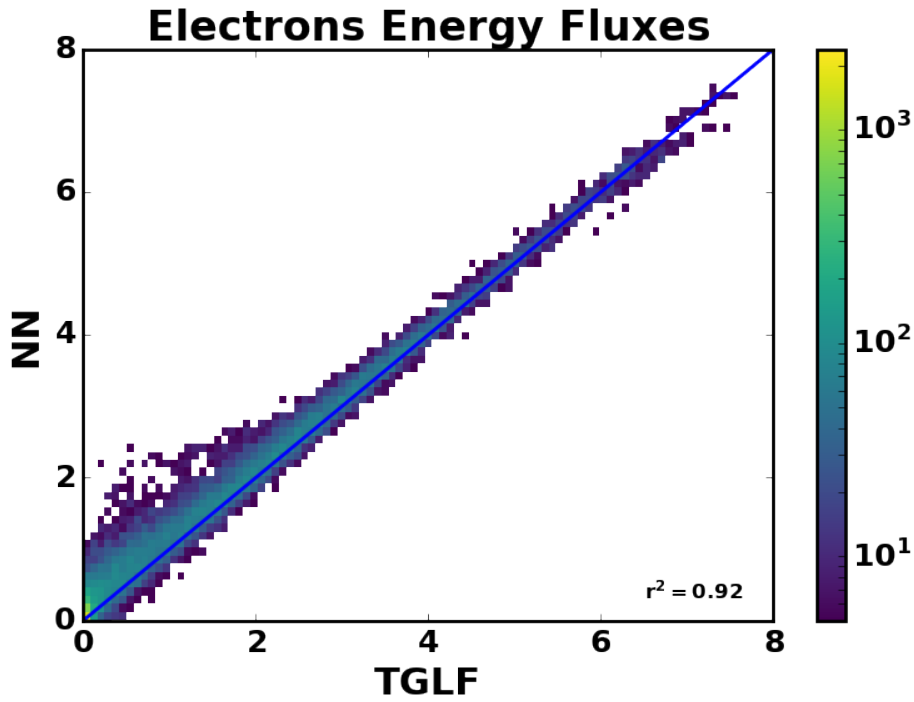


FIGURE 3.7: Electron energy fluxes computed with saturation rule obtained with neural network compared to TGLF fluxes.

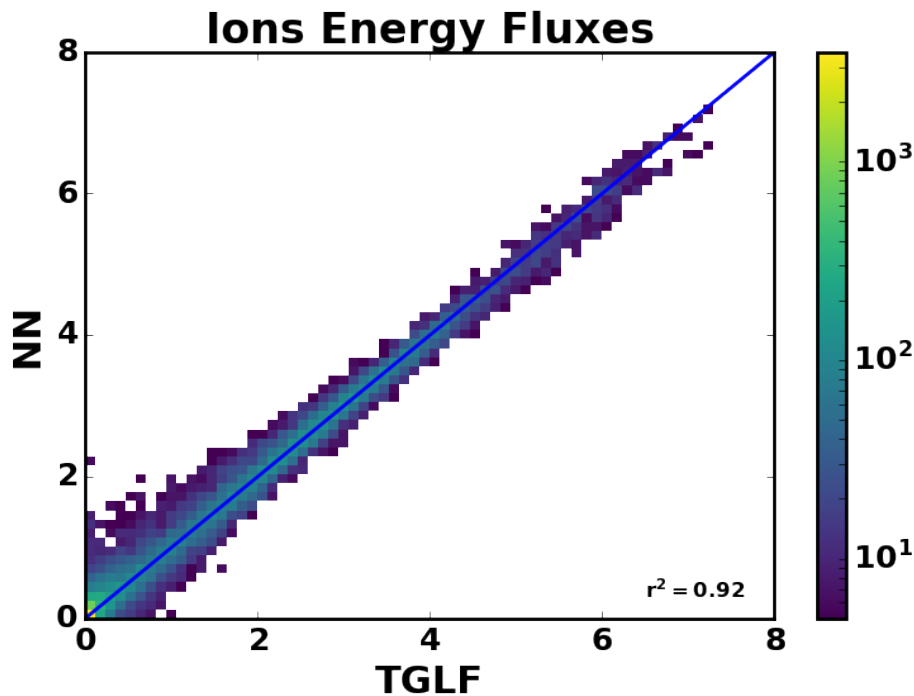


FIGURE 3.8: Ion energy fluxes computed with saturation rule obtained with neural network compared to TGLF fluxes.

The plots show a good agreement between the TGLF and the SATNN-multi fluxes. The value of the correlation coefficient $r^2 = 0.92$ (see [A](#)) underlines the capability of the neural network to combine the inputs of SAT0 to find a model that reproduce SAT0 itself.

This result is a benchmark useful to confirm the effectiveness of the algorithm implemented. Indeed, this comparison is used as validation of the neural network implementation.

3.3.2 Neural Network with SAT0 inputs

Once the model of the neural network is validated, the comparison with the experimental fluxes can be now analyzed.

The unique change with respect to the analysis explained in paragraph [3.3.1](#) is the set of target fluxes used in the error evaluation. The TGLF fluxes are now replaced with the experimental fluxes for the same cases contained in the database [2.3](#).

The error is computed minimizing the second term of the r^2 for both electrons and ions energy fluxes.(see [A](#))

Figures [3.9](#) and [3.10](#) show the regression of the experimental fluxes (x axis) and SATNN-multi fluxes (y-axis). The value of the $r^2 = 0.14$ means that the model works but the performance is not ideal.

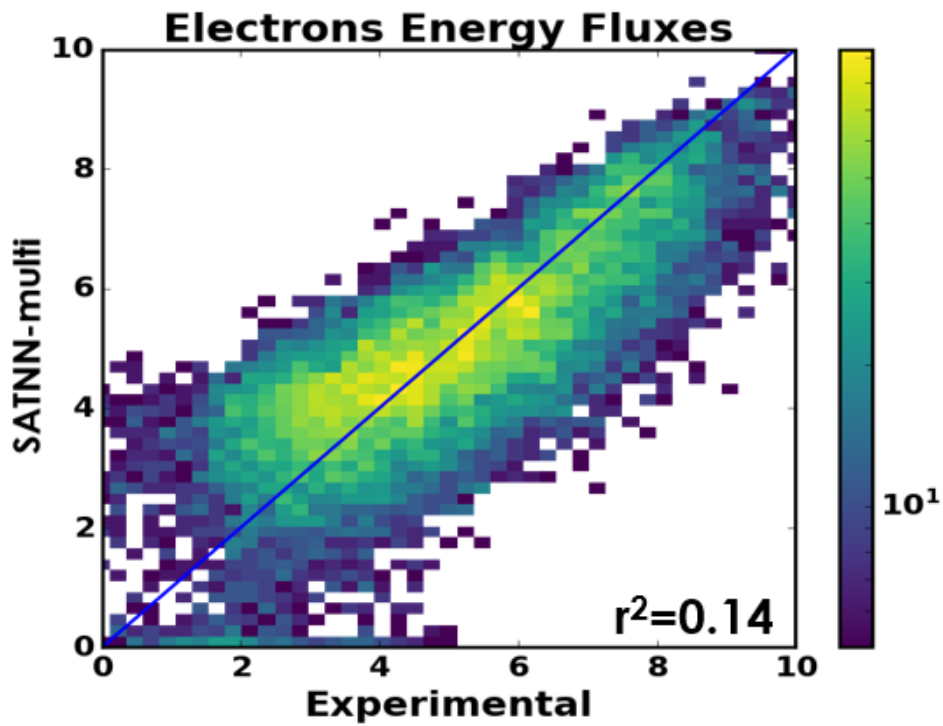


FIGURE 3.9: Electron energy fluxes computed with saturation rule obtained with SATNN-multi compared to experimental fluxes.

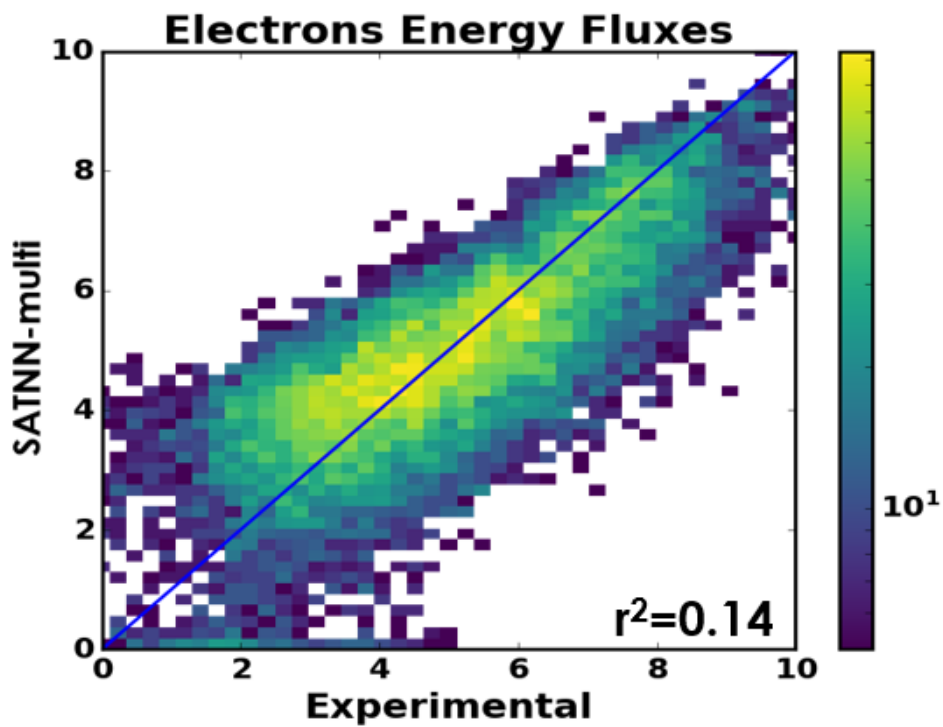


FIGURE 3.10: Ion energy fluxes computed with saturation rule obtained with SATNN-multi compared to experimental fluxes.

The SATNN-multi saturation rule fits better the experimental fluxes than SAT0, but the results are not yet satisfactory.

A different strategy for the neural network should be found to improve the investigation of the saturation rule. The results obtained with the SATNN-multi suggest that it is possible to change the model of SAT0 to obtain better results.

The functional form of SAT0 has been substituted with a group of neural network that find a better combination of the inputs in table 3.2 to fit the experimental fluxes.

Trying to go one step further from the SAT0 structure, the dependency on one single \hat{k}_y can be eliminated to find a global formulation of the saturation rule in which the value of one poloidal wavenumber can contribute to the calculation of the value of the saturation rule for other \hat{k}_y s. To follow this strategy the architecture of the neural network changed.

One single global neural network accept in input the same inputs of the 42 multi-neural network. This increased the speed-up of the training since only one single neural network has to update the weights that links the different nodes. The results of the global neural network for electron and ions are shown respectively in figures 3.11 and 3.12.

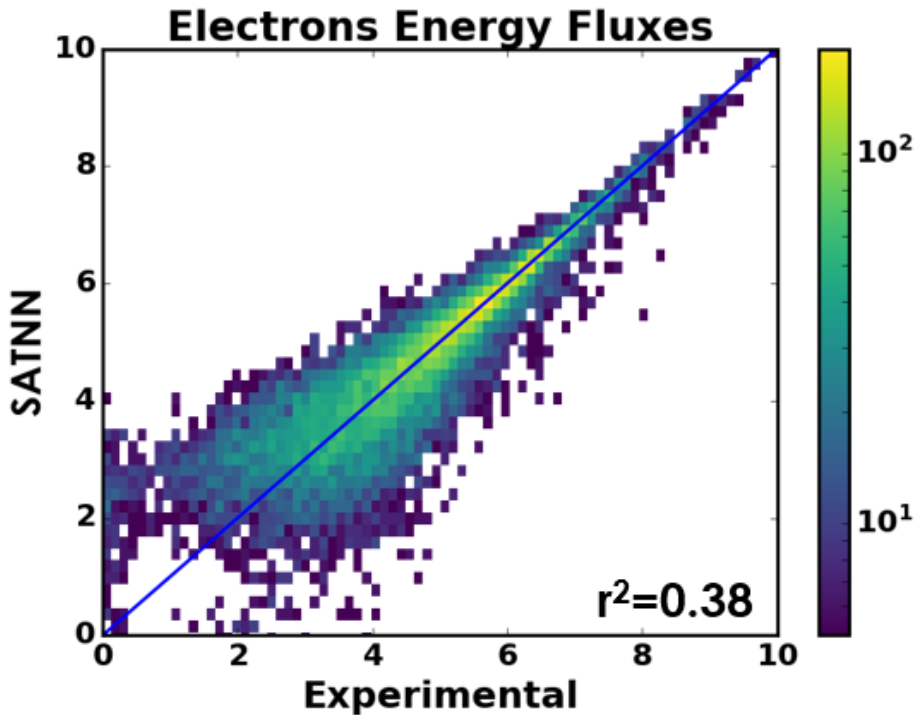


FIGURE 3.11: Electron energy fluxes computed with saturation rule obtained with SATNN compared to experimental fluxes.

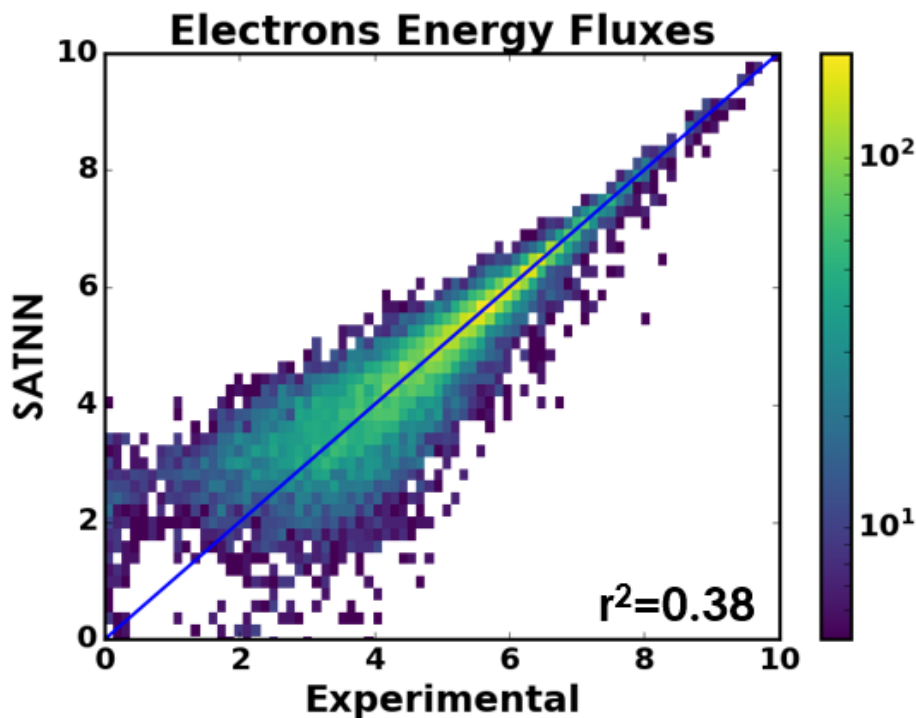


FIGURE 3.12: Ion energy fluxes computed with saturation rule obtained with SATNN compared to experimental fluxes.

The regression plots shows an improvement on the reproduction of the experimental fluxes. The values of the $r^2 = 0.38$ confirm the performance of global neural network with respect to the SATNN-multi.

3.3.3 Neural Networks with plasma parameter inputs

The good results discussed in paragraph 3.3.2 suggest that the functional form of SAT0 is not the best formulation of the saturation when the goal is to match the experimental fluxes.

Reducing the relationship between SAT0 and the saturation rule modelled with the neural network, the results improve. E.g. the elimination of the local nature increased the match of the two sets of fluxes compared.

Since SAT0 is not effective in the reproduction of the experimental fluxes, a set of parameters that characterize the plasma, used as input of TGLF, are added to the input of the neural network to model the saturation rule.

The inputs parameters are highlighted in table 3.3.

TABLE 3.3: Plasma Parameters

n_s/n_e	Normalized species density
T_i/T_e	Ion to electron temperature ratio
β_e	Kinetic to magnetic pressure ratio
λ_d/a	Normalized Debye length
δ	triangularity
κ	elongation
$r\dot{\kappa}$	normalized elongation shear
q	safety factor
a/L_{T_e}	Electron temperature scale length
a/L_{T_i}	Ion temperature scale length
a/L_{n_e}	Electron density scale length
a/L_{n_i}	Ion density scale length
r/a	Normalized minor radius
R/a	Normalized major radius
$r\dot{v}_\perp/c_s$	Normalized $E \times B$ velocity shear
$r\dot{v}_\parallel/c_s$	Normalized $E \times B$ velocity shear
$\nu_{ei}/a/c_s$	Normalized electron-ion collision frequency

A new training was performed on the SATNN-multi and on the SATNN using the same topologies discussed in paragraph 3.3.2.

For the multi-NN the regression plots for electrons and ions energy fluxes with respect to experimental fluxes are shown in figures 3.13 and 3.14. The values of r^2 are improved compared to the previous SATNN-multi trained using only the SAT0 parameters. The value increased to $r^2 = 0.59$.

For SATNN a similar consideration can be made. The value of r^2 increased up to 0.44. Figures 3.15 and 3.16 show the trends of the comparison of the energy fluxes.

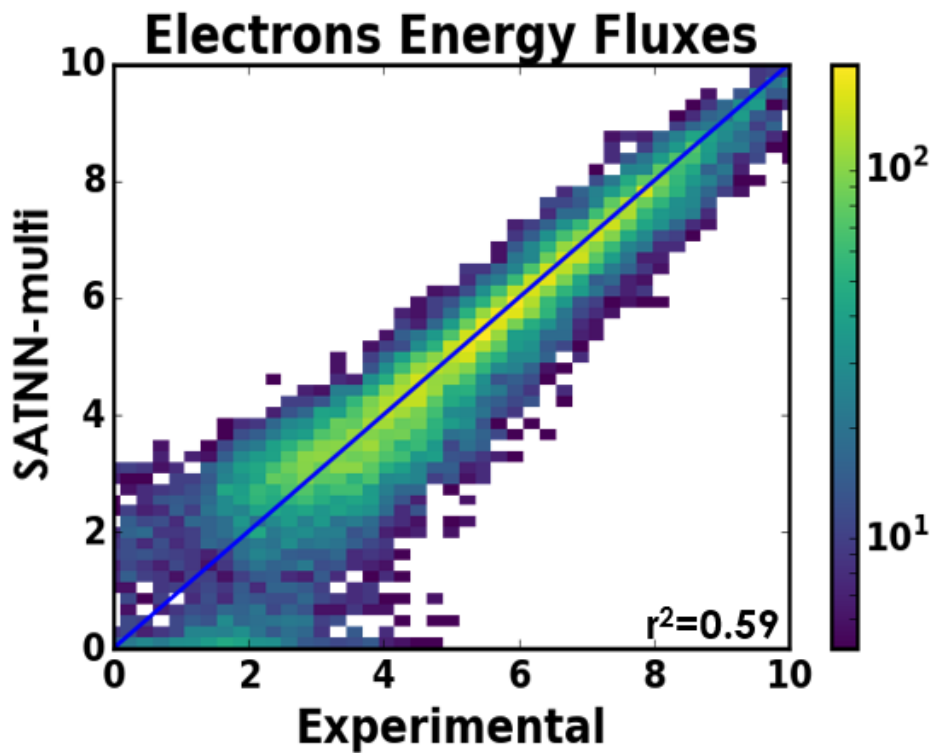


FIGURE 3.13: Electron energy fluxes computed with saturation rule obtained with SATNN-multi compared to experimental fluxes.

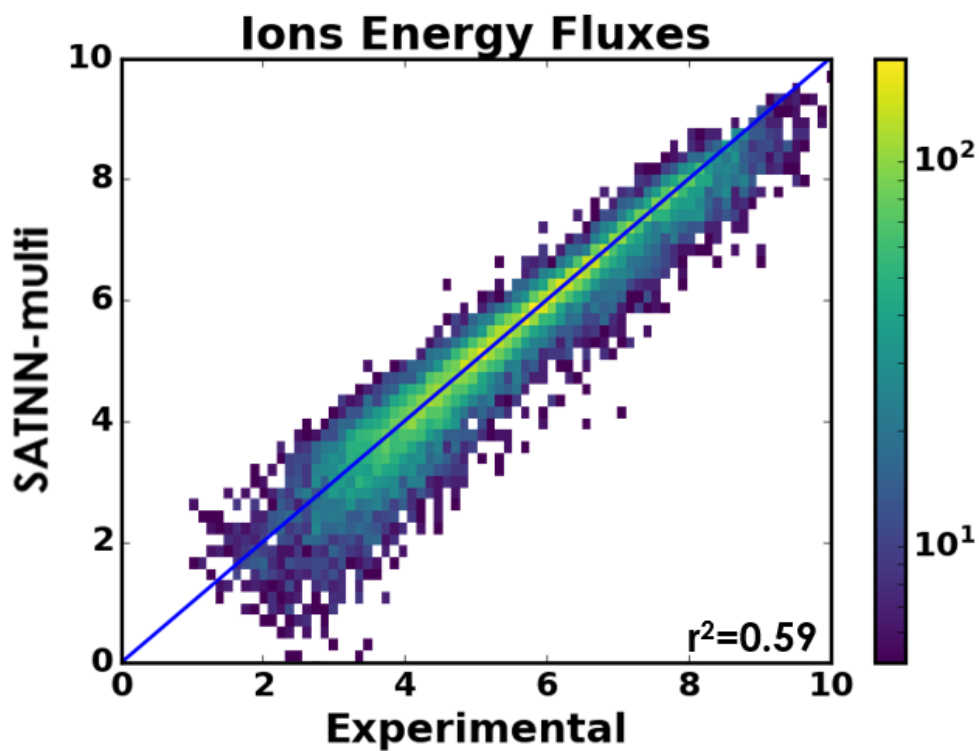


FIGURE 3.14: Ion energy fluxes computed with saturation rule obtained with SATNN-multi compared to experimental fluxes.

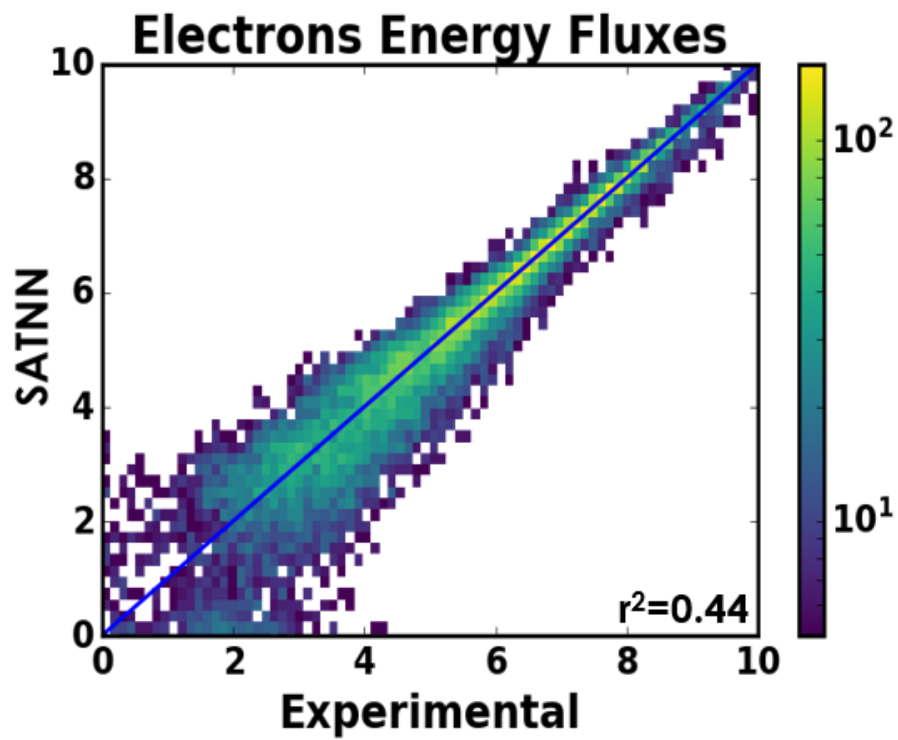


FIGURE 3.15: Electron energy fluxes computed with saturation rule obtained with SATNN compared to experimental fluxes.

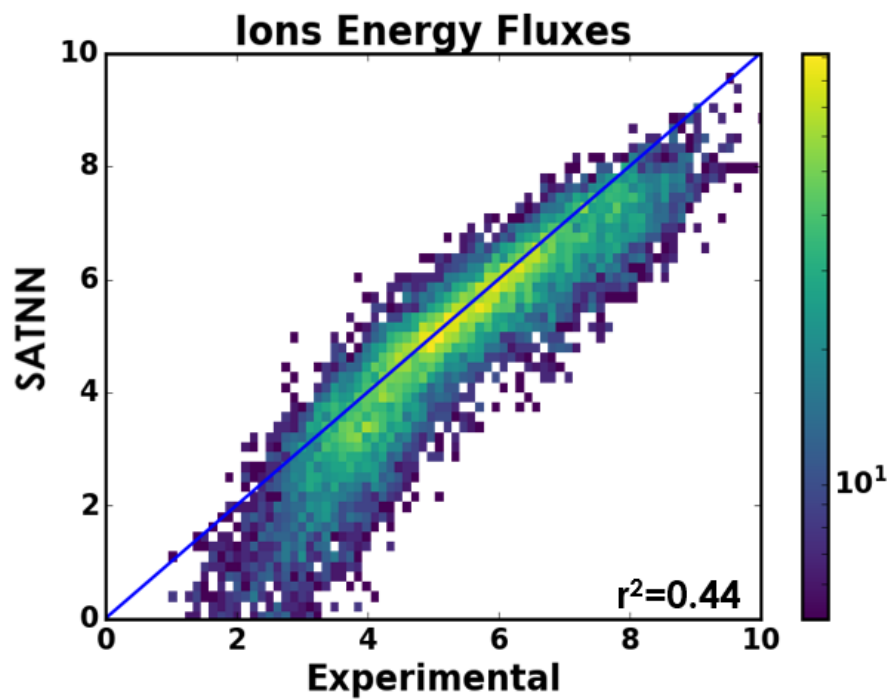


FIGURE 3.16: Ion energy fluxes computed with saturation rule obtained with SATNN compared to experimental fluxes.

One consideration on the last results is now discussed. The value of r^2 in the last two models of the saturation rule are respectively 0.59 and 0.44 for the SATNN-multi and the SATNN.

Although SATNN-multi model for the saturation rule has a better value of r^2 the performance, compared to SATNN, are worse. In fact, looking at a single case of the database, the spectrum of the saturation rule is plotted in figure 3.17:

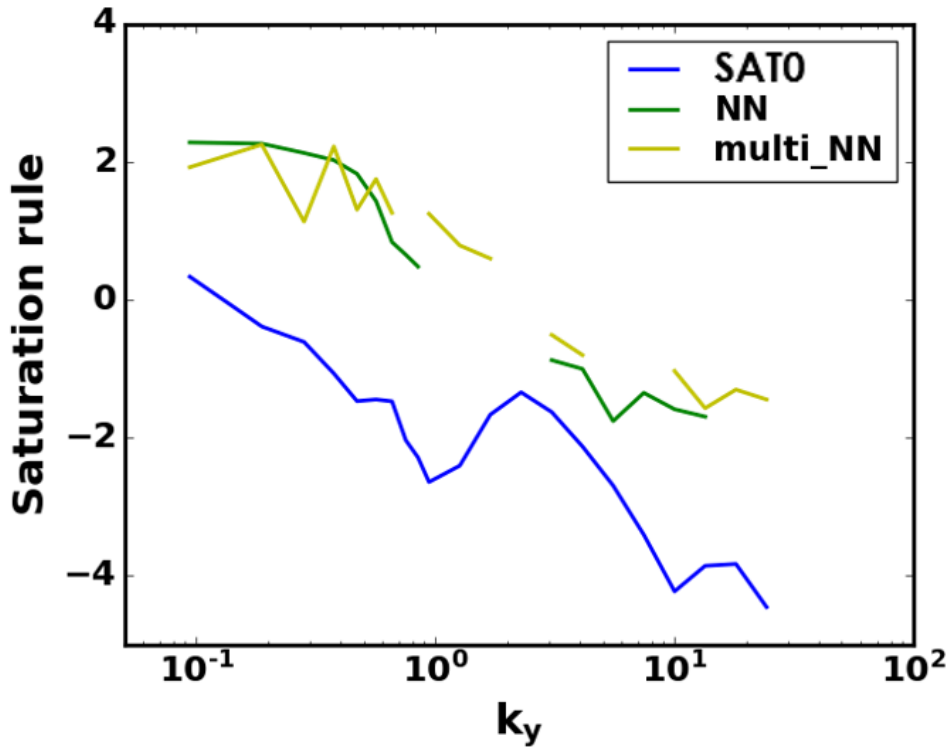


FIGURE 3.17: Behavior of different saturation rules studied.

SAT0, in blue, has a smaller value that will be discussed later.

Focusing attention on the yellow (SATNN-multi) and green (SATNN) lines, the two models have the same trend and order of magnitude but the SATNN-multi model is less smooth compared to the SATNN model.

Looking at SAT0, the spectrum of values is smooth and this leads to the conclusion that the smoothness of SATNN makes SATNN itself more reliable than SATNN-multi. The same behavior is noticed in all the other cases. Hence, even if the value of r^2 is smaller for SATNN, the performance (smoothness in wavenumber space) is better, confirming that a global formulation of the saturation rule should be used.

Chapter 4

Performances of the model and new saturation rule

The theoretical nature of TGLF led to a mismatch of the fluxes that it computes compared to the experimental fluxes. The saturation rule is used to obtain the fluxes, so a new model using the neural network is found in chapter 3. The results show a good reproduction of the experimental fluxes using the SATNN model and the plasma parameters 3.3 as inputs for the neural network. In this chapter the differences of the formulations are studied. The net growth rates are responsible for the underestimation of the fluxes and a semi-analytic formulation of the saturation rule is modeled to fill the shortfalls of the SATNN saturation rule.

4.1 Comparison of SAT0 and SATNN

In paragraph 3.1 the underestimation of the fluxes is introduced. A correlation exists between the underestimated fluxes and the value of the gradients.

The small values of TGLF fluxes occur when the gradients inside the plasma assume smaller values. More precisely, putting a threshold on the value of the fluxes at 0.01 (normalized fluxes) all the cases below the threshold occur when the normalized electron temperature gradient is smaller than 2 (*normalized gradient* = $\frac{a}{T} \frac{dT}{dr}$). 4.1

Figure 4.2(a) shows the behavior of SAT0 for all the cases in the database. Splitting the cases of high fluxes and small fluxes using the same criterion above mentioned, it can be noticed that, for the cases under the threshold, the values of SAT0 are two order of magnitude lower than the cases above the threshold.

Performing the same analysis on the values of saturation rule obtained with the SATNN model, the lower band is absent [see figure 4.3(d)] and the order of magnitude of the saturation rule for the cases under the threshold is the same as the cases above it. This means that the new model SATNN is able to correct the underprediction created by SAT0.

Focusing the analysis on two single cases, one in the zone with a smaller gradient and one in the zone of larger gradient, which correspond respectively to the group under and above the flux threshold, the saturation rule spectra are shown in figures 4.4 and 4.5.

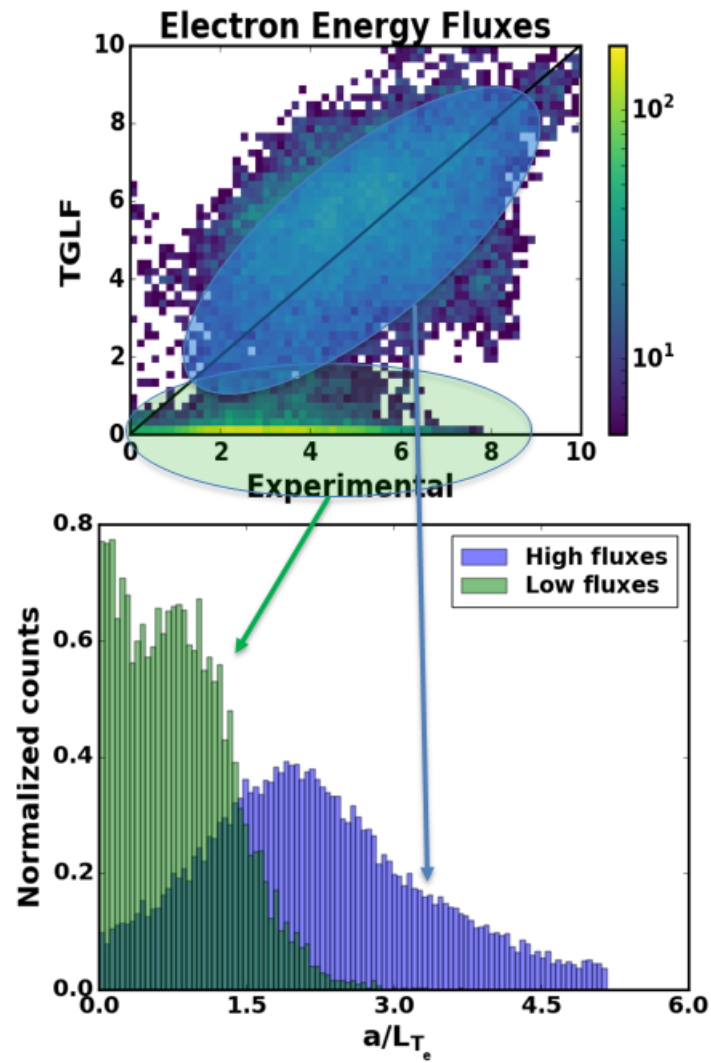


FIGURE 4.1: Highlight of the two different groups of energy fluxes and normalized distribution of the two group with respect to the electron temperature gradient.

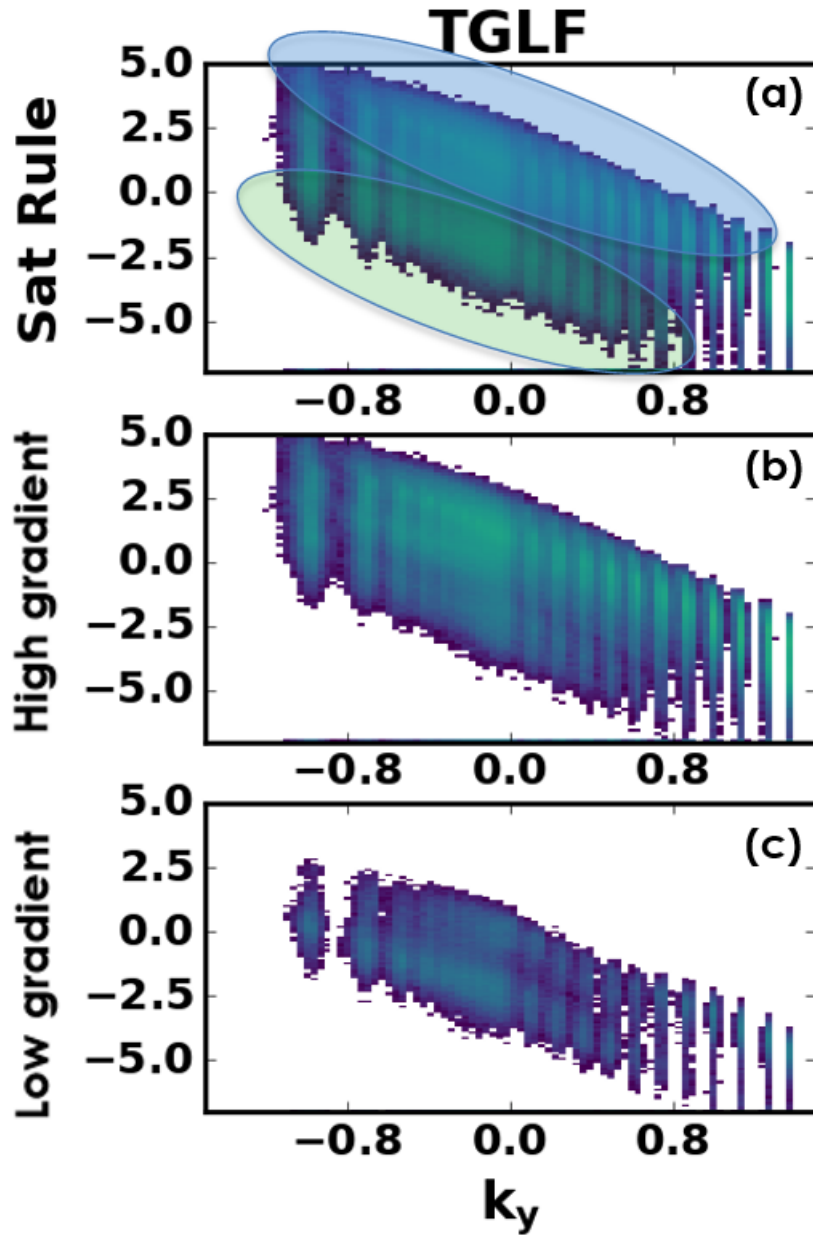


FIGURE 4.2: \log_{10} of saturation rule SAT0 for all the database cases (a), for the cases with high value of the flux (b) and for the cases with low value of the flux(c)

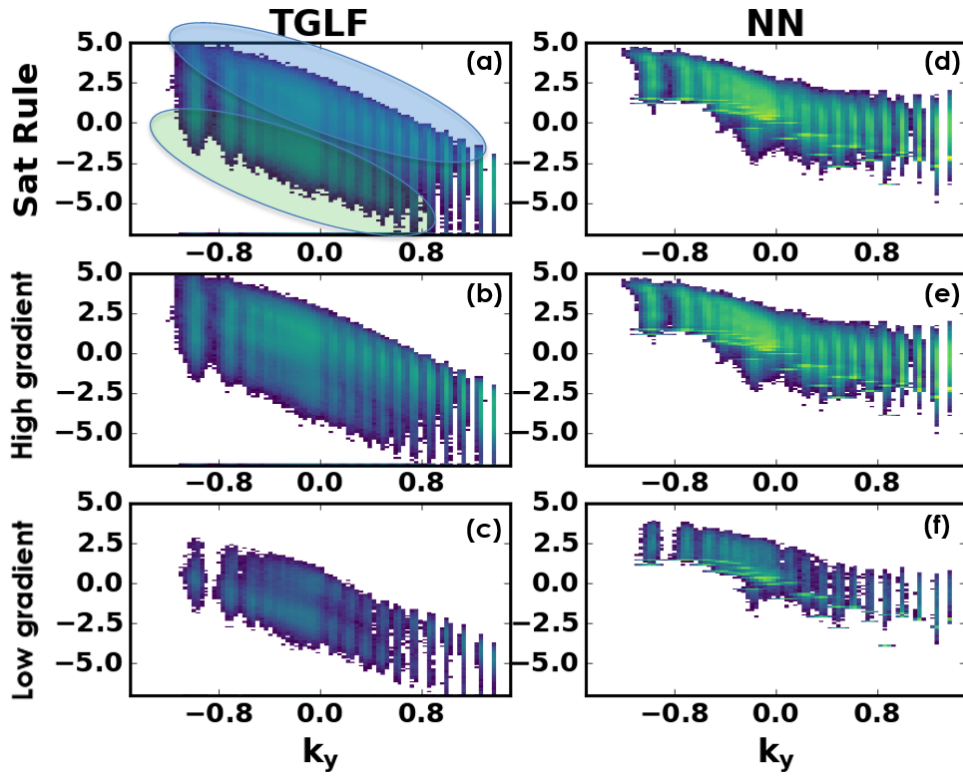


FIGURE 4.3: Saturation rules SAT0 (left) and SATNN (right) for all the database cases (a)(d), for the cases with high value of the flux (b)(e) and for the cases with low value of the flux(c)(f)

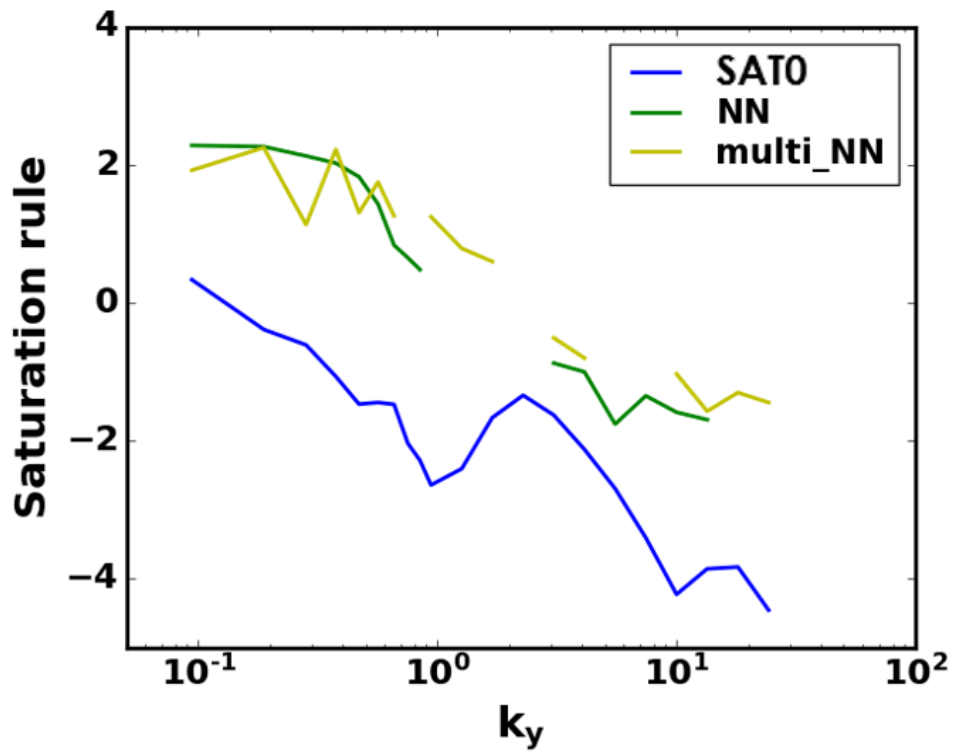


FIGURE 4.4: \log_{10} behavior of the different saturation rules studied for a case with small gradient.

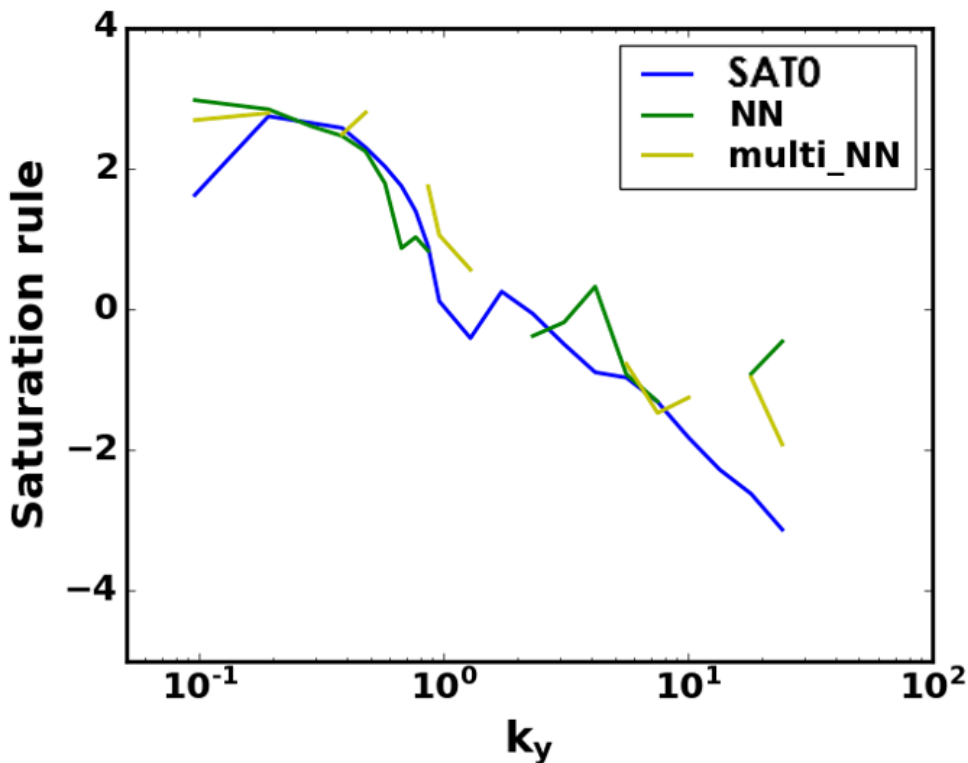


FIGURE 4.5: \log_{10} behavior of the different saturation rules studied for a case with high gradient.

Figure 4.4 shows one case when the fluxes are underpredicted. The value of the saturation rule is lower in SAT0 with respect to both SATNN-multi and SATNN. On the other hand, figure 4.5 shows one case with high value of flux. Here the order of magnitude of SAT0 is of the order of the neural network models. Further investigation is needed to find the causes that drop the saturation rule values of SAT0.

4.2 Causes of SAT0 shortfall

Having in mind that SAT0 is the cause of the underprediction of the fluxes when the gradients inside the plasmas have smaller values, the dependencies on the gradient of the terms inside the original TGLF saturation rule are explored.

$$\bar{V}^2 = C_{norm} \left(\frac{\rho_s \hat{\omega}_{d0}}{a \hat{k}_y} \right)^2 \left(1 + \frac{T_e}{T_i} \right)^2 (\bar{\gamma}_{net}^{C_1} + C_2 \bar{\gamma}_{net}) \frac{1}{\hat{k}_y^{C_3}}. \quad (4.1)$$

A strong dependency on \hat{k}_y and γ_{net} has been found. \hat{k}_y gives the slope to the function and is not responsible for the underestimation.

The growth rates γ_{net} , on the contrary, could cause the underestimation of SAT0. Plotting the values of the growth rates with respect to the electron temperature gradient, it can be noticed that for small values of the gradient the values of γ_{net} drop to zero exponentially characterizing the small values of the

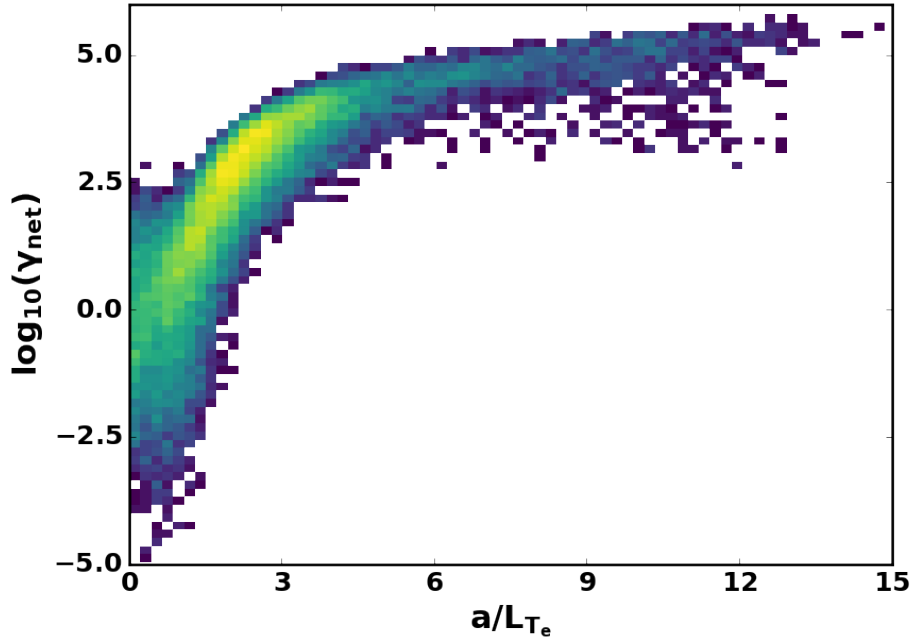


FIGURE 4.6: Growth rates computed by TGLF with respect to the gradient.

saturation rule above mentioned and, consequently, the underprediction of the fluxes.

4.3 New analytical saturation rule

The dependency of SAT0 on growth rates is the cause of TGLF underpredicting the experimental fluxes as noticed in the previous paragraph. In this paragraph a new raw functional form for the saturation rule is modeled trying to get rid of the growth rate as a contributor to the saturation rule. A strong dependency on \hat{k}_y can be seen in 4.2. More precisely, a dependence on $1/\hat{k}_y$ to a certain power is discovered, similar to the functional form of SAT0. In paragraph 4.1 in the last two figures 4.4 and 4.5 can be seen that some values of both SATNN and SATNN-multi can be negative and, because the plot is in logarithmic scale, the corresponding points are absent. To face this problem, in the numerator of the new formulation, a logarithm of \hat{k}_y is used. The structure of the new saturation rule is:

$$\bar{V}^2 = \frac{a(\dots) + b(\dots) \log_{10}(\hat{k}_y)}{\hat{k}_y^{c(\dots)}} \quad (4.2)$$

where a, b and c are sets of values obtained using a neural network. The input of the neural networks are only the plasma parameters highlighted in 3.3. At the end of the training, the model of the saturation rule is able to reproduce the experimental fluxes and the regression of the computed fluxes using the new

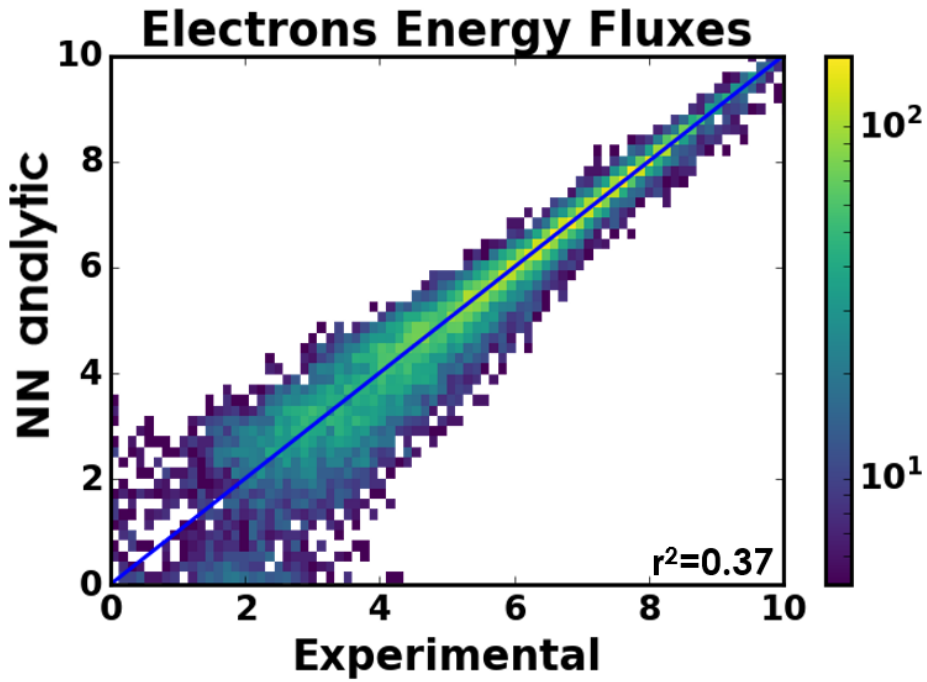


FIGURE 4.7: Electrons energy fluxes computed with the analytic saturation rule compared to the experimental fluxes.

analytical saturation rule and the experimental fluxes for electrons and ions are shown in figures 4.7 and 4.8.

The value of the coefficient of determination of the model is $r^2 = 0.37$. Even if the value of the r^2 is low the effectiveness of the new model can be evaluated looking at the same two cases analyzed in figures 4.4 and 4.5.

The new saturation rule reproduces the same trend as the SATNN-multi and SATNN models. The same order of magnitude and the same slope are obtained with all three neural network models of the saturation rule. But the SATNN-multi and SATNN models show some shortfall in the strength of the results. As already mentioned, some values are missed because the plot has a logarithmic scale for the y-axis and the negative values are not plotted. These negative values have no physical meaning but will lead to negative fluxes; in our dataset of experimental fluxes all the values are positive, a negative evaluation of the saturation rule will result in an error of the model. The analytic saturation rule is always definite positive, thanks to the nature of the functional form that prevents the model from computing negative values.

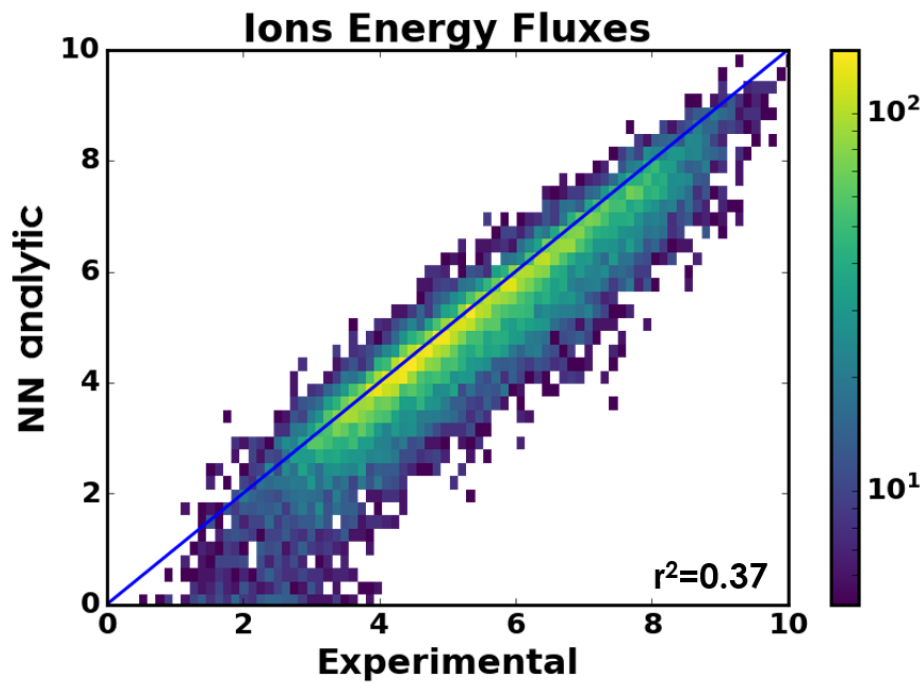


FIGURE 4.8: Ions energy fluxes computed with the analytic saturation rule compared to the experimental fluxes.

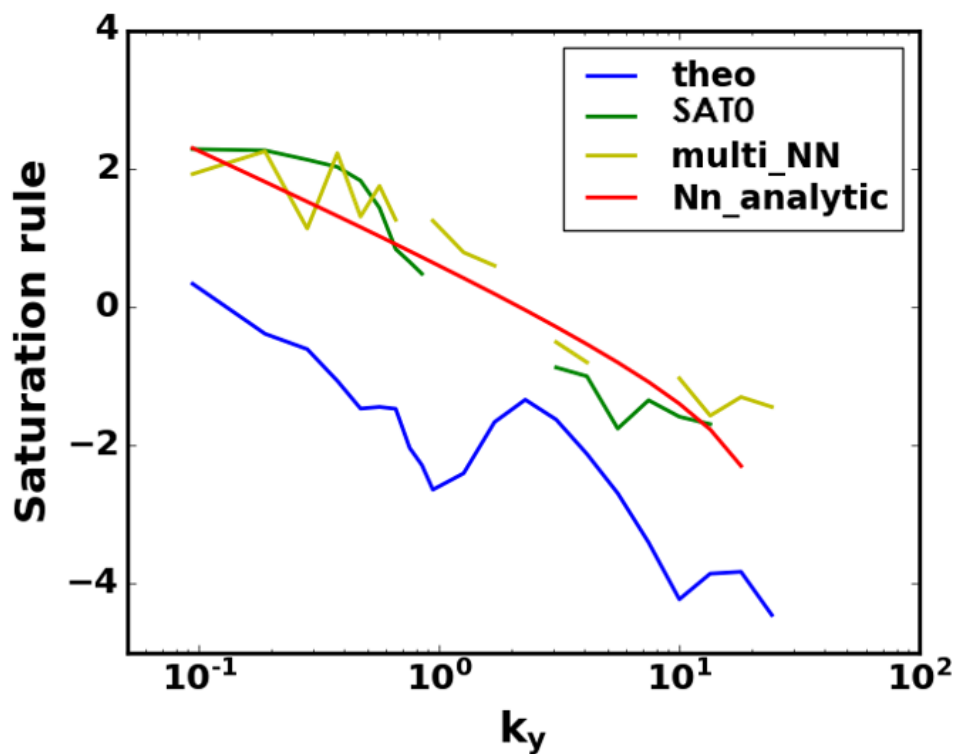


FIGURE 4.9: Behavior of the different saturation rules studied for a case with small gradient.

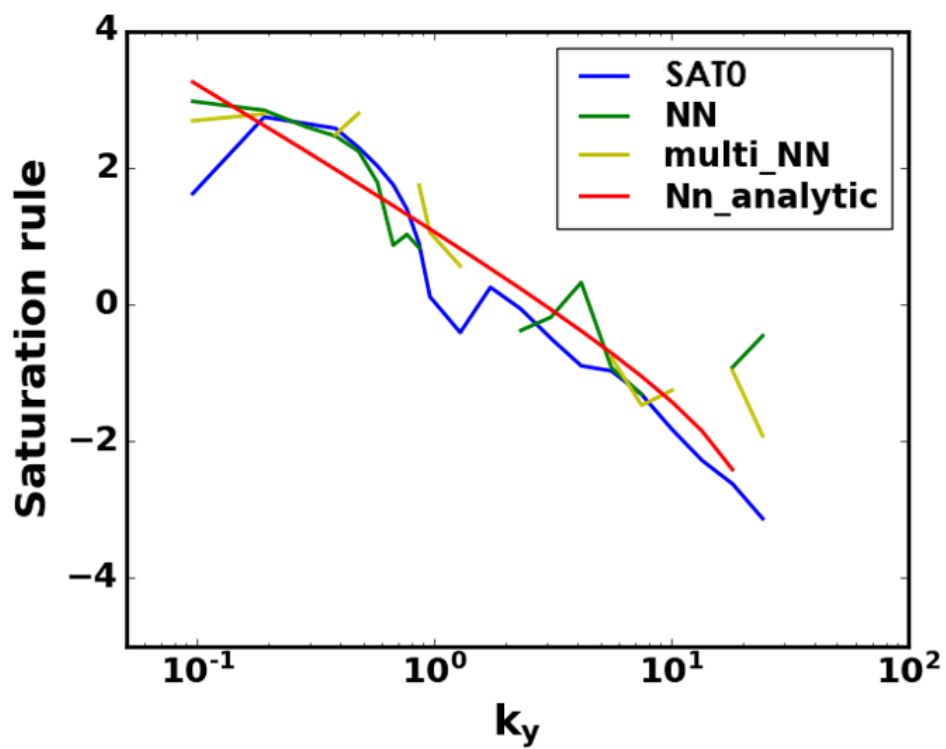


FIGURE 4.10: Behavior of the different saturation rules studied for a case with high gradient.

Chapter 5

Conclusions

Nuclear fusion is an ambitious project pursued by a big number of researchers and scientists in the world. Improvement on the knowledge and technologies requires big effort and better understanding of the phenomenology that drive the fusion reactions.

Transport in the plasma in the fusion field is an important topic, one of the pillars of this discipline. To study, model, and understand the physics inside tokamaks different tools have been developed. As discussed in the first part of the thesis, different solvers are able to run simulations that compute the fluxes, the turbulence, and the state of the plasma. These codes are powerful but expensive in terms of computational cost.

Reduced models were developed to face the problem of the computational cost with a speedup of several orders of magnitude.[13] TGLF is a transport solver able to compute the fluxes in the plasma using a quasi-linear approximation of the non linear turbulent models. To link the quasi-linear quantities to the non linear turbulent fluxes uses a saturation rule calibrated to fit a set of reference non-linear simulations. Some shortfall occurs when the TGLF energy fluxes are compared to the experimental fluxes. To reduce the discrepancies between the two fluxes the saturation rule was studied to investigate why it fails and how a new model can be found.

Using machine learning via a neural network approach a new model of the saturation rule able to reproduce the experimental fluxes was found. These results were analyzed to understand the reasons of the mismatching of the TGLF fluxes and the experimental fluxes. One of the reasons is the local nature of the saturation rule SAT0 that does not allow the coupling of the contributions of different scales of the poloidal wavenumber \hat{k}_y . The second, and most important, reason is the dependency on the growth rates. The values of the growth rates drop exponentially when the values of the gradients are small inside the tokamak. To face the problem a new functional form of the saturation rule has been developed and tuned with the use of a neural network that has as input the same plasma parameters used as input to TGLF. The outputs of the neural network are three quantities here called a, b and c. The next step of the analysis could be to find a correlation between these three values and the inputs of the model and if it exist try to substitute the term a, b or c with the corresponding parameters using the characteristics of the dependency (power, logarithm...) to find a fully analytical expression that does not depend on a neural network. This points out the power of the neural network in modeling a saturation rule and the utility of this approach to drive the theoretical research.

One further observation is made looking at the figures 5.1 and 5.2.

As can be seen in the figure, there are still values of the fluxes computed with the new analytic saturation rule that underestimate the experimental fluxes. A fast analysis on the QL weights, that is not part of this thesis, shows that these quantities drop exponentially when the gradients are small, behaving similarly to the growth rates.

More future work could be the investigation of these quantities to improve the overall performances of TGLF. This project opened different topics that can be studied in future works, stating that the neural network can be used in the analysis of a theoretical problem to produce results or hints that can be exploited to improve the knowledge and the understanding of the plasma physics.

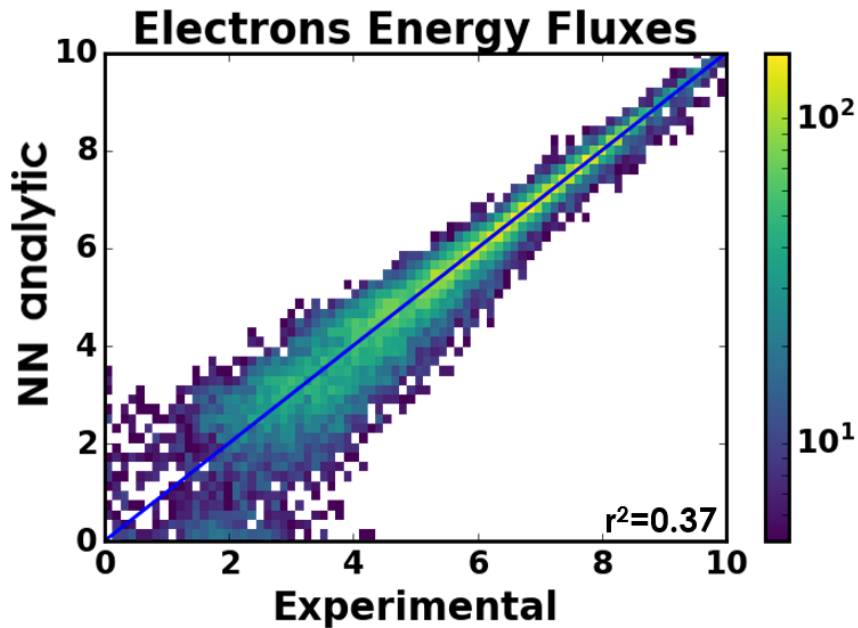


FIGURE 5.1: Electrons energy fluxes computed with the analytic saturation rule compared to the experimental fluxes.

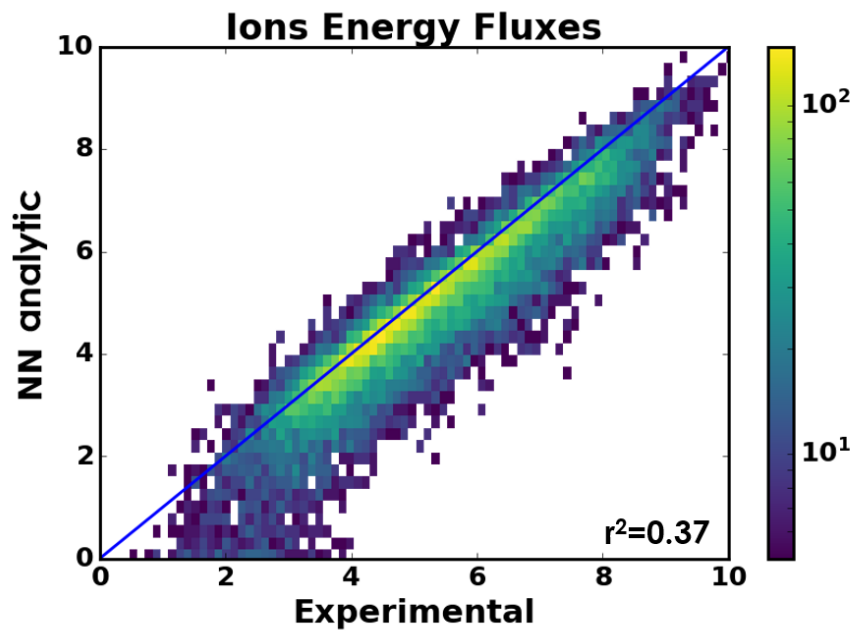


FIGURE 5.2: Ions energy fluxes computed with the analytic saturation rule compared to the experimental fluxes.

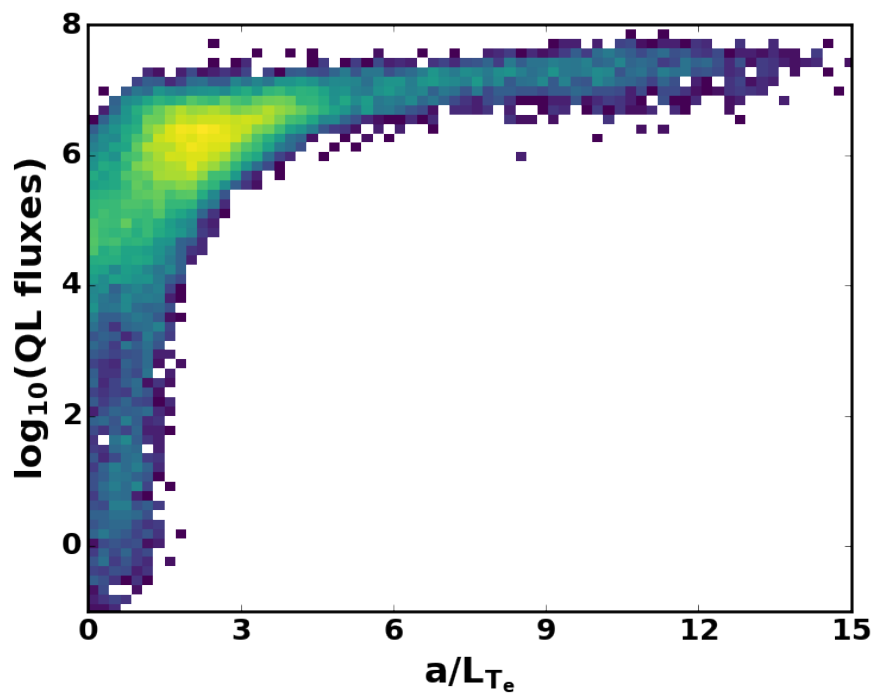


FIGURE 5.3: QL weights computed by TGLF with respect to the gradient.

Bibliography

- [1] J. Candy and R. E. Waltz. “Anomalous Transport Scaling in the DIII-D Tokamak Matched by Supercomputer Simulation”. In: *Phys. Rev. Lett.* 91 (4 2003), p. 045001. DOI: [10.1103/PhysRevLett.91.045001](https://doi.org/10.1103/PhysRevLett.91.045001). URL: <https://link.aps.org/doi/10.1103/PhysRevLett.91.045001>.
- [2] J. Candy, R. E. Waltz, and W. Dorland. “The local limit of global gyrokinetic simulations”. In: *Physics of Plasmas* 11.5 (2004), pp. L25–L28. DOI: [10.1063/1.1695358](https://doi.org/10.1063/1.1695358). eprint: <https://doi.org/10.1063/1.1695358>. URL: <https://doi.org/10.1063/1.1695358>.
- [3] J. Candy and R.E. Waltz. “An Eulerian gyrokinetic-Maxwell solver”. In: *Journal of Computational Physics* 186.2 (2003), pp. 545–581. ISSN: 0021-9991. DOI: [https://doi.org/10.1016/S0021-9991\(03\)00079-2](https://doi.org/10.1016/S0021-9991(03)00079-2). URL: <http://www.sciencedirect.com/science/article/pii/S0021999103000792>.
- [4] *DIII-D experiment main page*. 2019. URL: <https://fusion.gat.com/global/diii-d/home>.
- [5] J.P. Freidberg. *Plasma Physics and Fusion Energy*. Cambridge University Press, 2008. ISBN: 9781139462150. URL: <https://books.google.it/books?id=Vyoe88GEVz4C>.
- [6] hyperphysics. *Coulomb barrier*. 2019. URL: <http://hyperphysics.phy-astr.gsu.edu/hbase/NucEne/coubar.html>.
- [7] J. Kinsey. *The GYRO Nonlinear Gyrokinetic Simulation Database*. Jan. 2008.
- [8] J. E. Kinsey, G. M. Staebler, and R. E. Waltz. “The first transport code simulations using the trapped gyro-Landau-fluid model”. In: *Physics of Plasmas* 15.5 (2008), p. 055908. DOI: [10.1063/1.2889008](https://doi.org/10.1063/1.2889008). eprint: <https://doi.org/10.1063/1.2889008>. URL: <https://doi.org/10.1063/1.2889008>.
- [9] Martin Kubic. “Review of plasma parameters of the JET tokamak in various regimes of its operation”. MA thesis. Czech Technical University, 2007.
- [10] N. C. Logan et al. “OMFIT Tokamak Profile Data Fitting and Physics Analysis”. In: *Fusion Science and Technology* 74.1-2 (2018), pp. 125–134. DOI: [10.1080/15361055.2017.1386943](https://doi.org/10.1080/15361055.2017.1386943). eprint: <https://doi.org/10.1080/15361055.2017.1386943>. URL: <https://doi.org/10.1080/15361055.2017.1386943>.
- [11] James M McDonough. “Introductory lectures on turbulence: physics, mathematics and modeling”. In: (2007).

- [12] O. Meneghini et al. “Integrated modeling applications for tokamak experiments with OMFIT”. In: *Nuclear Fusion* 55.8 (2015), p. 083008. URL: <http://iopscience.iop.org/article/10.1088/0029-5515/55/8/083008/meta>.
- [13] O. Meneghini et al. “Self-consistent core-pedestal transport simulations with neural network accelerated models”. In: *Nuclear Fusion* 57.8 (July 2017), p. 086034. DOI: 10.1088/1741-4326/aa7776. URL: <https://doi.org/10.1088/1741-4326/aa7776>.
- [14] G. M. Staebler, J. E. Kinsey, and R. E. Waltz. “A theory-based transport model with comprehensive physics”. In: *Physics of Plasmas* 14.5 (2007), p. 055909. DOI: 10.1063/1.2436852. eprint: <https://doi.org/10.1063/1.2436852>. URL: <https://doi.org/10.1063/1.2436852>.
- [15] G. M. Staebler, J. E. Kinsey, and R. E. Waltz. “Gyro-Landau fluid equations for trapped and passing particles”. In: *Physics of Plasmas* 12.10 (2005), p. 102508. DOI: 10.1063/1.2044587. eprint: <https://doi.org/10.1063/1.2044587>. URL: <https://doi.org/10.1063/1.2044587>.
- [16] Gregorio Luigi Trevisan. “Development of 2D/3D equilibrium codes for magnetically confined fusion experiments”. PhD thesis. Università degli Studi di Padova, 2013.
- [17] Wikipedia. *Coefficient of determination* - *Wikipedia, The Free Encyclopedia*. 2019. URL: https://en.wikipedia.org/wiki/Coefficient_of_determination.
- [18] Wikipedia. *Nuclear binding energy* - *Wikipedia, The Free Encyclopedia*. 2019. URL: https://en.wikipedia.org/wiki/Nuclear_binding_energy.
- [19] Wikipedia. *Proton-proton chain reaction* - *Wikipedia, The Free Encyclopedia*. 2019. URL: https://en.wikipedia.org/wiki/Proton-proton_chain_reaction.
- [20] Wikipedia. *Tokamak* - *Wikipedia, The Free Encyclopedia*. 2019. URL: <https://en.wikipedia.org/wiki/Tokamak>.
- [21] Wikipedia. *Wendelstein 7-X* - *Wikipedia, The Free Encyclopedia*. 2019. URL: <https://it.wikipedia.org/wiki/>.

Appendix A

Coefficient of determination

In statistics, the coefficient of determination, indicated with the symbols R^2 or r^2 , is a measure of how well a model can reproduce or predict the desired results. It is widely used in linear regression analysis: its value varies between 0 and 1. A value near 0 indicates that the model does not produce reliable outcomes compared to the data analyzed. The closer to 1 the value is, the more reliable is the model. The value 1 means that the model perfectly fits the data and can be used for future prediction. The definition of the *coefficient of determination* is formulated below. Having a set of n known data that can be indicated with y_1, \dots, y_n and a set of predicted or computed values f_1, \dots, f_n , some quantities can be defined [17]

mean value of the known data

$$\bar{y} = \frac{1}{n} \sum_{i=1}^n y_i;$$

total sum of squares computed as the sum of the square of each known value minus the mean value

$$S_{tot} = \sum_{i=1}^n (y_i - \bar{y})^2;$$

residual sum of squares computed as the sum of the square of each known value minus the corresponding predicted value

$$S_{res} = \sum_{i=1}^n (y_i - f_i)^2.$$

The *coefficient of determination* is defined as

$$R^2 = 1 - \frac{S_{res}}{S_{tot}} = 1 - \frac{\sum_{i=1}^n (y_i - f_i)^2}{\sum_{i=1}^n (y_i - \bar{y})^2}. \quad (\text{A.1})$$

In this project, for the optimization of the neural network, the last term of equation (A.1) was used as the quantity to minimize. In fact, minimizing $\frac{\sum_{i=1}^n (y_i - f_i)^2}{\sum_{i=1}^n (y_i - \bar{y})^2}$ the coefficient of determination assumes higher values, which means better performances of the neural network model.